Aberration-free imaging of inelastic-scattering spectra with x-ray echo spectrometers

Manuel Sánchez del Río[1,*] and Yuri Shvyd'ko[2,†]

[1]*ESRF, The European Synchrotron, Grenoble, France*
[2]*Advanced Photon Source, Argonne National Laboratory, Argonne, Illinois 60439, USA*

We study conditions for aberration-free imaging of inelastic x-ray-scattering (IXS) spectra with x-ray echo spectrometers. Aberration-free imaging is essential for achieving instrumental functions with high resolution and high contrast. Computational ray tracing is applied to a thorough analysis of a 0.1 meV/0.07-nm^{-1}-resolution echo-type IXS spectrometer operating with 9-keV x rays. We show that IXS spectra imaged by the x-ray echo spectrometer that uses lenses for the collimating and focusing optics are free of aberrations. When grazing incidence mirrors (paraboloidal, parabolic Kirkpatrick-Baez, or parabolic Montel) are used instead of the lenses, the imaging system reveals some defocus aberration that depends on the inelastic energy transfer. However, the aberration-free images can be still recorded in a plane that is tilted with respect to the optical axis. This distortion can be thus fully compensated by inclining appropriately the x-ray imaging detector, which simultaneously improves its spatial resolution. A full simulation of imaging IXS spectra from a realistic sample demonstrates the excellent performance of the proposed designs.

I. INTRODUCTION

X-ray echo spectroscopy [1], a space-domain counterpart of neutron spin echo [2], was introduced recently to overcome the limitations in spectral resolution and weak signals of the traditional inelastic hard-x-ray-scattering (IXS) probes. X-ray echo spectroscopy is an extension into the hard-x-ray domain of the approach proposed [3] and demonstrated in the soft-x-ray domain [4]. X-ray echo is refocusing the defocused x-ray source image. Defocusing and refocusing systems are the main components of x-ray echo spectrometers. They are composed of focusing and dispersing optical elements, where the latter are asymmetrically cut crystals in Bragg diffraction. The optical elements have to be complemented by the x-ray source, sample, and x-ray position-sensitive detector, as schematically shown in Fig. 1. Refocusing takes place only when the defocusing and the refocusing systems compose a time-reversed pair. This implies that a virtual source placed into the detector plane produces the defocused image in the sample plane with the same linear dispersion rate as the real source.

When the defocused x rays are scattered inelastically from the sample with an energy transfer ε, they pass through the refocusing system that refocuses them on the detector, but with a lateral shift with respect to the optical axis that is proportional to ε [see Fig. 1(v_i)]. This property enables echo spectrometers to image IXS spectra with a spectral resolution solely determined by the sharpness of the refocused image of the source, and completely independent of the spectral composition of x rays incident on the sample. The spectral resolution of x-ray echo spectrometers is therefore decoupled

from the spectrometer bandwidth, x-ray monochromatization is not required, and the IXS refocusing (imaging) system is broadband. These features of echo spectrometers are in a striking contrast to present-day narrow-band scanning IXS spectrometers (see [5] for a review), the spectral resolution of which is determined by the smallness of the monochromator and analyzer bandwidths. As a result, broadband imaging echo-type IXS spectrometers have the potential of increasing the signal strength by orders of magnitude, thus reducing acquisition times and substantially improving spectral resolution.

The ability of the refocusing system to produce sharp and undeformed images for each inelastic ε component is critical for achieving the high-resolution and high-contrast instrumental functions of echo-type spectrometers. This is, however, a challenge, because the defocused source image on the sample and the refocused IXS image on the detector are spread laterally with respect to the optical axis. Therefore, x-ray echo spectrometers must be truly aberration-free imaging systems capable of producing sharp images when the focusing elements are illuminated both on axis and off axis.

The theory of x-ray echo spectrometers developed in [1,6] is based on paraxial analytical ray tracing, which uses ray transfer matrix analysis. It predicts aberration-free imaging, provided ideal (perfectly focusing and nonabsorbing) parabolic x-ray lenses are used, which make sure that the collimating and focusing elements form a truly imaging optical system. This conclusion is also supported by computational wave propagation studies [7] performed with SRW code [8] for a 0.1-meV-resolution x-ray echo spectrometer with the parameters from [1].

Real parabolic x-ray compound refractive lenses (CRLs) [9] have small effective geometrical aperture for the x-ray echo spectrometers because of photoabsorption. Curved grazing incidence mirrors may feature much larger

---

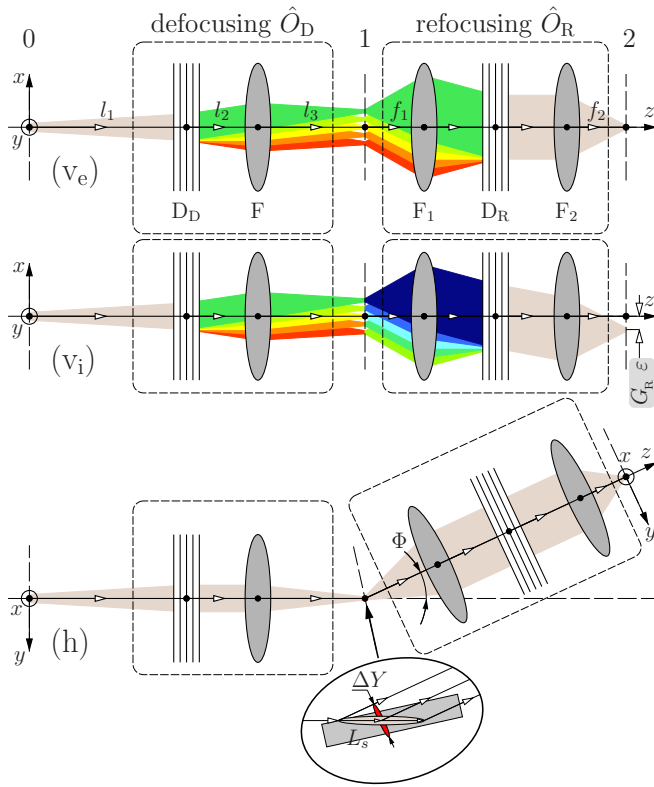*srio@esrf.eu
†shvydko@anl.gov

FIG. 1. Optical scheme of an x-ray echo spectrometer, composed of the defocusing $\hat{O}_D$ and refocusing $\hat{O}_R$ dispersing-focusing systems; the x-ray source in reference plane 0; the sample in reference plane 1; and the pixel detector in reference plane 2. The spectrometer is shown in the vertical (x, z) dispersion plane for elastic (v_e) and inelastic (v_i) scattering cases, as well as in the horizontal (y, z) nondispersive scattering plane (h) with the refocusing system at a scattering angle Φ defining the momentum transfer $Q = 2K \sin(\Phi/2)$ in scattering of a photon with an angular wave number K. See text for more details.

apertures. However, mirrors are not good imaging devices. The Abbe sine condition, which defines the constraints that any perfect imaging system must comply with, states in particular the impossibility of building an imaging system with a single mirror. At least two reflectors are needed. In the x-ray regime, the use of Wolter-type grazing incidence mirror pairs [10,11] may ensure perfect imaging. The Abbe sine condition in connection with the refocusing system of x-ray echo spectrometers made up of a pair of paraboloidal mirrors with the dispersing system in between was discussed in [6] limited, however, to one-dimensional (1D) mirrors.

The present paper aims at identifying conditions for aberration-free IXS imaging by echo-type IXS spectrometers with real three-dimensional (3D) mirror and lens systems. It uses geometrical three-dimensional ray tracing of systems composed of crystals, mirrors, or lenses, including calculation of crystal reflectivity and lens absorption. The calculations are performed using the x-ray optics modeling package SHADOW [12] and its graphical user interface ShadowOUI [13] available in the software suite for x-ray optics and synchrotron beamline simulations OASYS [14].

The paper is organized as follows. In Sec. II we present the basic principles of x-ray echo spectrometers, as well as the optical design and parameters of the studied spectrometer with a 0.1-meV spectral and a 0.07-nm^{-1} momentum-transfer resolution. In Sec. III we present results of studies of IXS imaging with lenses, using both ideal focusing lenses and a full simulation of an array of real paraboloidal compound refractive lenses. Section IV is devoted to studies of IXS imaging using grazing incidence mirror systems, starting first with a case of imaging elastic signals in Sec. IV A and then imaging inelastic signals in Sec. IV B, where image aberrations produced in the image plane (Sec. IV B 1) are corrected if recorded by a detector in an oblique plane (Sec. IV B 2). Effects of glancing angle of incidence and mirrors' slope errors on the spectral resolution are discussed in Secs. IV C and IV D, respectively. Full simulations of imaging IXS spectra from realistic samples are performed in Sec. V to verify the performance of the proposed design.

II. PRINCIPLES, OPTICAL DESIGN, AND PARAMETERS OF X-RAY ECHO SPECTROMETERS

Here, we review the principles of x-ray echo spectrometers, and the optical scheme defining in detail the configuration and elements used in the numerical simulations.

A. Basic principles and optical scheme

The optical scheme of the x-ray echo spectrometer considered here is shown in Fig. 1. Its performance was discussed in detail and substantiated by analytical ray tracing in [1,6].

As a result of propagation through the defocusing system $\hat{O}_D$, x rays from the source with a vertical size Δx_0 in reference plane 0 are focused on the sample in reference plane 1 with an image size $\Delta x_1 = A_D \Delta x_0$ (A_D is a magnification factor), albeit, with the focal spot location dispersed in vertical direction x for different spectral components with a linear dispersion rate G_D.

All spectral components of the defocused source image can be refocused into a single spot (echo) with a size $\Delta x_2 = A_R \Delta x_1$ in the detector reference plane 2 by propagation through the refocusing system $\hat{O}_R$, provided it is a time-reversed counterpart of the defocusing system $\hat{O}_D$. The latter means that x rays from a virtual source of size Δx_2 in the detector plane being propagated in the reverse direction produce on the sample exactly the same defocused image as the image by the defocusing system. This is expressed by the refocusing condition

$$G_D + G_R/A_R = 0, \tag{1}$$

where G_R is a linear dispersion rate and A_R is a magnification factor of the refocusing system.

If inelastic scattering takes place on the sample with an energy transfer ε, the dispersed signal is still refocused into a tight echo signal, but laterally shifted by $\delta x_2 = G_R \varepsilon$ in the detector plane, as shown schematically in Fig. 1(v_i). This effect enables imaging IXS spectra with an energy resolution

$$\Delta \varepsilon = \Delta x_2/|G_R| \equiv \Delta x_1/|G_D|, \tag{2}$$

TABLE I. Global optical parameters of an x-ray echo spectrometer with a 0.1-meV spectral and a 0.07-nm^{-1} momentum-transfer resolution (see Fig. 1 for the optical scheme and the text for notations). The following parameters are fixed: monochromatic source size on the sample $\Delta x_1 = 5\ \mu$m, the source to sample distance $l = l_1 + l_2 + l_3$, and the focal lengths f and f_1. Other parameters are chosen to ensure the 0.1-meV design spectral resolution, Eqs. (2) and (6), to fulfill the refocusing condition, Eq. (1) and Eqs. (3) and (4). The central photon energy of the incident x rays on the sample is $E_0 = 9137.01$ eV, defined by (008) Bragg reflections from the Si crystals in the dispersing elements (see Figs. 2 and 3 and Table VI of Appendix A).

Defocusing system									Refocusing system						
G_D	l	l_1	l_2	l_3	A_D	$\mathcal{D}_{\cup_D}$	$b_{\cup_D}$	f	G_R	A_R	f_1	$\frac{\mathcal{D}_{\cup_R}}{b_{\cup_R}}$	$b_{\cup_R}$	f_2	$A_D A_R$
$(\frac{\mu m}{meV})$	(m)	(m)	(m)	(m)		$(\frac{\mu rad}{meV})$		(m)	$(\frac{\mu m}{meV})$		(m)	$(\frac{\mu rad}{meV})$		(m)	
∓ 50	35	32.55	0.73	1.72	−0.095	−31.7	1.96	1.45	∓ 50	−1.0	0.4	−125	0.27	1.471	0.095

where $\Delta\varepsilon$ corresponds to an energy transfer resulting in a lateral shift δx_2 that is equal to the image size Δx_2. One of the major purposes of the paper is to verify by detailed numerical simulations the capability of x-ray echo spectrometers to image IXS spectra with the spectral resolution given by Eq. (2).

The main components of the defocusing and refocusing systems are the dispersing elements D_D and D_R and focusing elements F, F_1, and F_2. The dispersing elements are characterized by the cumulative angular dispersion rates $\mathcal{D}_{\cup_D}$ and $\mathcal{D}_{\cup_R}$, cumulative asymmetry parameters $b_{\cup_D}$ and $b_{\cup_R}$, and spectral bandwidths ΔE_D and ΔE_R, respectively (see [1,6] for details). The focusing elements are characterized by the focal lengths f, f_1, and f_2. These parameters determine [1,6] the linear dispersion rate G_D and the magnification factor A_D of the defocusing system

$$A_D = -\frac{\sigma_D}{b_{\cup_D}}\frac{l_3}{l_{12}}, \quad G_D = \sigma_D \mathcal{D}_{\cup_D}\frac{l_3 l_1}{b_{\cup_D}^2 l_{12}}, \tag{3}$$

$$\frac{1}{f} = \frac{1}{l_{12}} + \frac{1}{l_3}, \quad l_{12} = \frac{l_1}{b_{\cup_D}^2} + l_2 \tag{4}$$

and of the refocusing system

$$G_R = \sigma_R \mathcal{D}_{\cup_R} f_2, \quad A_R = -\frac{b_{\cup_R} f_2}{f_1}. \tag{5}$$

Compared to [1,6], we use here additional parameters $\sigma_X = +1$ if lenses are used as focusing elements, or alternatively $\sigma_X = -1$ for mirrors. Here $X = D$ or R.

Using Eq. (5), the spectral resolution $\Delta\varepsilon$ given by Eq. (2) can be equivalently expressed through the parameters of the refocusing system as

$$\Delta\varepsilon = \frac{|b_{\cup_R}|}{|\mathcal{D}_{\cup_R}|}\frac{\Delta x_1}{f_1}. \tag{6}$$

In the present paper we are studying a particular case of an x-ray echo spectrometer with a 0.1-meV spectral and a 0.07-nm^{-1} momentum-transfer resolution employing 9.1-keV x rays with design parameters provided in [6]. The global optical parameters of the x-ray echo spectrometer are summarized in Table I and discussed in the following sections.

B. From source to sample: Defocusing system

The vertical source size is typically $\Delta x_0 \simeq 25\ \mu$m [full width at half maximum (FWHM)] for state-of-the-art undulator synchrotron radiation sources. Assuming a focusing system with a magnification factor $|A_D| \simeq 0.1$, we expect

for the monochromatic beam size on the sample $\Delta x_1 = |A_D|\Delta x_0 \simeq 2.5\ \mu$m. Because the high-heat-load monochromator (installed upstream of the defocusing system, not shown in Fig. 1) may degrade the wavefront, we use in our simulations a more conservative value $\Delta x_1 = 5\ \mu$m. This value together with the design spectral resolution $\Delta\varepsilon = 0.1$ meV of the x-ray echo spectrometer determine via Eq. (2) the required value of the linear dispersion rate $|G_D| = 50\ \mu$m/meV.

Focusing element F should possess properties of the true imaging system. We assume it to be a paraboloidal CRL, in a good approximation of the truly imaging optic [9]. Its focal length $f = 1.446$ m can be realized using 17 double-convex 2D Beryllium lenses of 200-μm radius of curvature. This chosen configuration gives an effective geometrical aperture of 660 μm, comparable to the size of the intercepted undulator beam.

In our paper, we fix the value of f as well as the source-to-sample distance $l = l_1 + l_2 + l_3 = 35$ m. The values of other parameters of the defocusing system (see Table I), such as $\mathcal{D}_{\cup_D}$, $b_{\cup_D}$, l_1, l_2, l_3, and A_D, are not unique but are chosen to be practical and to meet the constraints imposed by Eqs. (1)–(4).

The dispersing element D_D has to be chosen to meet the values of $\mathcal{D}_{\cup_D}$ and $b_{\cup_D}$ provided in Table I. The required big angular dispersion rate $\mathcal{D}_{\cup_D} = -31.7\ \mu$rad/meV can be achieved only by using multicrystal systems featuring the enhancement effect of angular dispersion [15,16].[1] Considered in the present paper is a four-crystal dispersing element discussed in detail in [6]. Its optical scheme and spectral transmission function are also shown in Fig. 2.

C. From sample to detector: Refocusing system

The refocusing system is composed of a pair of focusing elements F_1 and F_2, and a dispersing element D_R placed in between (see Fig. 1).

---

[1]Diffraction gratings are not practical dispersing elements in the hard-x-ray regime. Instead, crystals in Bragg diffraction can function as gratings, dispersing x rays into spectral fans with photons of different energies propagating at different angles [17–19]. The grating effect takes place only in asymmetric Bragg diffraction, with the diffracting atomic planes at a nonzero angle $\eta \neq 0$ to the entrance crystal surface. Bragg diffraction ensures high reflectivity, while the asymmetric cut results in electron-density periodic modulation along the crystal surface responsible for the grating effect of angular dispersion.
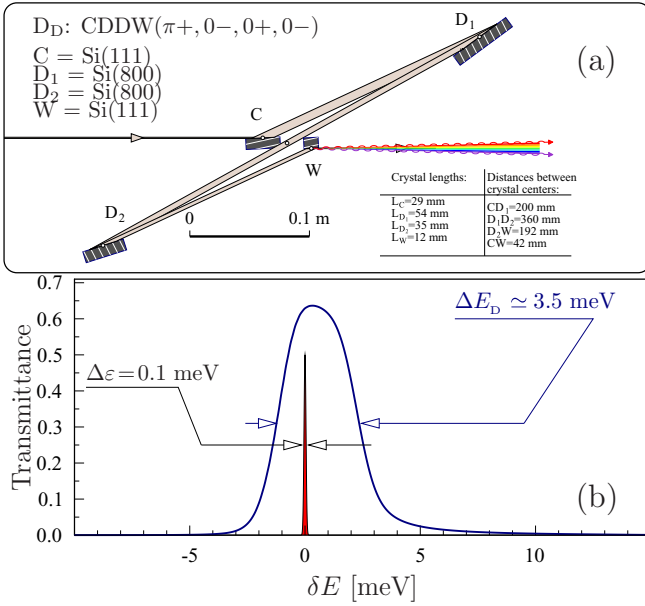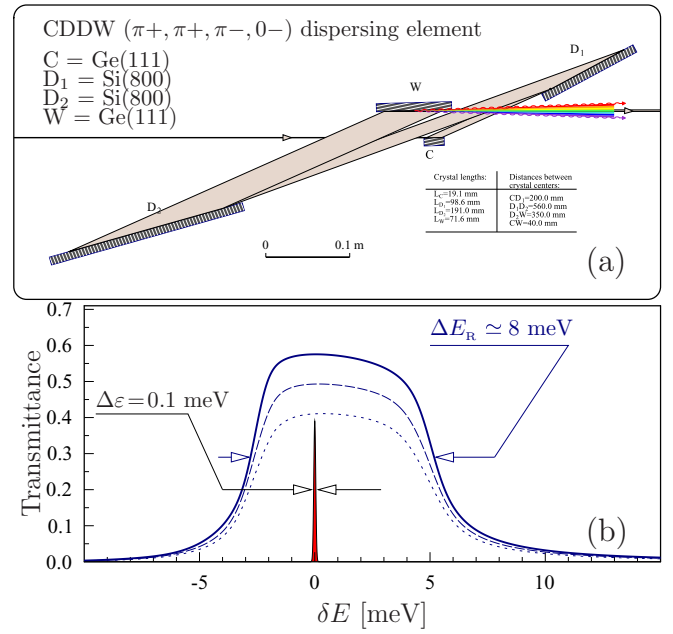
FIG. 2. In-line four-crystal CDDW-type x-ray dispersing element in a $(\pi+, 0-, 0+, 0-)$ configuration (a) and its spectral transmittance function (b) calculated for the incident beam divergence of 20 μrad. With the crystal parameters provided in [6] and in Table VI of Appendix A, the optic features a spectral transmission function with a $\Delta E_D = 3.5$-meV bandwidth (b), a cumulative angular dispersion rate $\mathcal{D}_{\cup_D} = -32$ μrad/meV, and a cumulative asymmetry factor $b_{\cup_D} = 2$ appropriate for dispersing element D_D of the defocusing system $\hat{O}_D$. The sharp red line in panel (b) indicates the 0.1-meV design spectral resolution.

The focal length of F_1 is chosen to be $f_1 = 0.4$ m, defined by the desired momentum-transfer resolution of $\Delta Q = 0.07$ nm^{-1} (see below). According to Eq. (6), this value of f_1 together with the design spectral resolution $\Delta\varepsilon = 0.1$ meV and the fixed value of the secondary monochromatic source size $\Delta x_1 = 5$ μm require that $\mathcal{D}_{\cup_R}/b_{\cup_R} = -125$ μrad/meV. The negative sign results from Eqs. (1) and (5). A four-crystal dispersing element with the required value of $\mathcal{D}_{\cup_R}/b_{\cup_R}$ was discussed in detail in [6]. Its optical scheme and spectral transmission function are also shown in Fig. 3.

The refocusing system is designed to provide 1:1 imaging (magnification factor $A_R = -1$) of the secondary source in the intermediate image plane 1 to image plane 2. This is favored by the Abbe sine condition (see discussion in [6] for details). This condition along with the previously defined values of f_1 and $b_{\cup_R}$ require $f_2 = 1.471$ m [see Eq. (5)]. In fact, the significance of the 1:1 magnification for aberration-free imaging of the IXS spectra is one of the central questions to be addressed by numerical simulations. Deviations from 1:1 imaging will be studied as well. The specific case of $A_R = -1$ requires $G_R = G_D = -50$ μm/meV and $\Delta x_2 = |A_D|\Delta x_0 \equiv \Delta x_1 = 5$ μm.

We study IXS imaging with different types of focusing elements F_1 and F_2: ideal lenses, 2D paraboloidal compound refractive lenses [9], 2D paraboloidal mirrors [20], or compound 2D mirror systems composed of 1D parabolic mirrors, such as Kirkpatrick-Baez (KB) [21] or Montel [22]. The mirrors are considered to be coated with laterally graded

FIG. 3. In-line four-crystal CDDW-type x-ray dispersing element in a $(\pi+, \pi+, \pi-, 0-)$ scattering configuration (a) and its spectral transmittance function (b) calculated for the incident beam divergence of 100 μrad (bold), 200 μrad (dotted), and 300 μrad (dashed). With the crystal parameters provided in [6] and in Table VI of Appendix A, the optic features a $\Delta E_R = 8$-meV bandwidth (b), a cumulative angular dispersion rate $\mathcal{D}_{\cup_R} = -34.2$ μrad/meV, a cumulative asymmetry factor $b_{\cup_R} = 0.27$, and $\mathcal{D}_{\cup_R}/b_{\cup_R} = -125.5$ μrad/meV, appropriate for dispersing element D_R of the refocusing system $\hat{O}_R$. The sharp line in panel (b) presents the 0.1-meV design spectral resolution $\Delta\epsilon$ of the x-ray echo spectrometer.

multilayers similar to those used in [23,24], providing a large glancing angle of incidence $\varphi \simeq 20$–30 mrad. Due to the large φ, the mirrors are compact, have a large geometrical aperture, and most importantly mitigate aberrations, as discussed in [6]. Impacts of the magnitude of φ and of the mirrors' slope errors on the IXS imaging will be studied.

D. Description of the sample, a secondary source for the refocusing system

X rays scattered from the sample are seen by the refocusing system as emanating from a secondary three-dimensional source. Studies [1,6,7] show that the performance of the refocusing system is relatively insensitive to the secondary source position along the optical axis. In particular, the tolerance on the position variation is at least a few millimeters in the present case of the 0.1-meV spectrometer. Therefore, if the sample thickness is much smaller, the secondary source can be considered with high accuracy to be flat and distributed only in plane (x, y). Such an approximation is used here.

The defocusing system focuses each spectral component E to a spot of a vertical size Δx_1 [see Figs. 1(v_e)–1(v_i)], with the locations linearly dispersed as
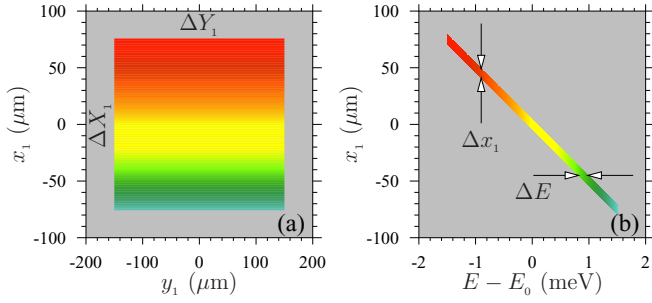
$$x_1(E) = G_D(E - E_0). \tag{7}$$

FIG. 4. (a) Virtual secondary source in reference sample plane 1 featuring photon energy dispersion in the vertical (x) direction with a linear dispersion rate $G_D = -50$ μm/meV. Source dimensions are $\Delta X = 150$ μm and $\Delta Y = 300$ μm. (b) Each horizontal line is a source of photons with a Gaussian spectral spread of $\Delta E = 0.1$ meV (FWHM). Each monochromatic component has a vertical Gaussian spread (monochromatic source size) of $\Delta x_1 = 5$ μm (FWHM).

In the elastic-scattering process, the photon energy of the secondary source is the same as that of the incident one, as indicated in Fig. 1(v_e). To simulate inelastic scattering with an energy transfer ε, we modify the energy of the x ray scattered by the sample as

$$E_0 \rightarrow E_0 + \varepsilon. \tag{8}$$

This presentation may mean that inelastic x-ray scattering with an energy transfer ε takes place in all scattering points simultaneously, as indicated in Fig. 1(v_i). This is not actually the case. However, this presentation is still valid if a time-averaged picture is assumed.

Because the angular acceptance of the refocusing system is limited to $\Delta\theta_R \simeq 260$ μrad [6], it can "see" only $\Delta\theta_R f_1 \simeq 100$ μm of the secondary source. We restrict, therefore, the total vertical size of the secondary source in our simulations to $\Delta X_1 = 150$ μm [see Fig. 4(a)]. This corresponds to a maximal spectral variation of $E - E_0 = \pm 1.5$ meV in the incident beam [see Fig. 4(b)].

If the scattering angle Φ is small [see Fig. 1(h)], the horizontal secondary source size is equal to the horizontal focal spot size on the sample, which can be just a few micrometers. However, with a finite penetration length L_s, the horizontal secondary source size $\Delta Y_1 = L_s \sin \Phi$ grows with Φ, as shown in the inset of Fig. 1(h). For practical reasons, which cover many cases, we assume in our simulations $\Delta Y_1 = 300$ μm.

Each point on the sample is a secondary source emitting isotropically (a spherical wave). But only a small part of the radiation will be accepted by the refocusing system (defined by the angular aperture of the system and possible use of secondary slits to control the momentum resolution). Here we limit the angular spread of the photons from the sample to 1.5 mrad in both the vertical Υ_v and horizontal Υ_h planes. This is consistent with the desired momentum-transfer resolution $\Delta Q = \Upsilon Q = 0.07$ nm^{-1} for the 0.1-meV spectrometer, where $\Upsilon = \max[\Upsilon_v, \Upsilon_h]$.

III. IXS IMAGING WITH LENSES

In the first step, we study how the extended two-dimensional x-ray source dispersed in the vertical direction
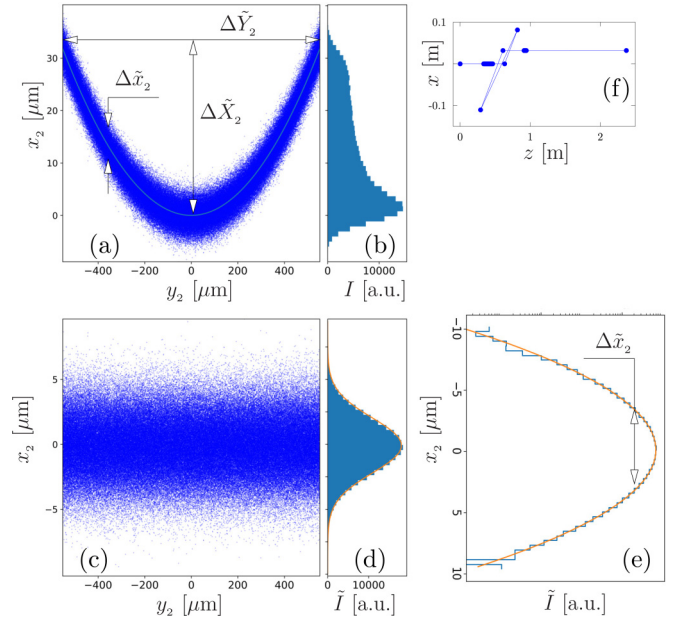
FIG. 5. (a) Cross section of the beam in image plane 2 rendered by the refocusing system composed of two ideal lenses and the CDDW dispersing element in between. The solid line represents a parabolic fit to the beam profile. (b) Vertical profile $I(x_2)$ obtained from panel (a) by integration over the horizontal coordinate y_2. (c) Beam cross section of panel (a) with the parabolic fit removed. (d) Vertical profile $\tilde{I}(x_2)$ obtained from panel (c) with a Gaussian fit (brown line). (e) Vertical profile $\tilde{I}(x_2)$ of panel (c) shown on the logarithmic scale. (f) Side view of the beam trajectory (optical axis). Angular apertures $\Upsilon_h = \Upsilon_v = 1.5$ mrad.

in reference plane 1 (see Figs. 1 and 4) is imaged in reference plane 2 by the refocusing system composed of nonabsorbing perfect paraboloidal lenses used as the collimating F_1 and focusing F_2 optical elements and of the CDDW dispersing element in between.

According to Fig. 1, we expect the refocusing system to focus all vertically dispersed monochromatic components into one spot, with the linear dispersion annihilated. In the perfect case, the vertical distribution should be Gaussian with a width Δx_2 equal to the monochromatic source size $\Delta x_1 = 5$ μm, assuming the designed 1:1 imaging in the vertical plane, which takes into account the combined effect of lenses and crystals ($A_R = -b_{\cup_R} f_2 / f_1 = -1$). The source image size in the horizontal direction is defined by the focal lengths of the lenses only: the magnification factor is $f_2/f_1 = 3.678$, thus the image size in the horizontal plane is $\Delta Y_2 = \Delta Y_1(f_2/f_1) = 1103$ μm. This picture turns out, however, to be incomplete.

Figure 5(a) shows the cross section of the beam calculated in image plane 2 in the case of elastic scattering ($\varepsilon = 0$), related to Fig. 1(v_e). Its horizontal width $\Delta \tilde{Y}_2$ agrees with ΔY_2 (we use tildes throughout the paper to indicate values calculated numerically). The vertical profile at any y_2 has a distribution which fits perfectly to the Gaussian function with a width $\Delta \tilde{x}_2 \simeq 4.95$ μm (FWHM), which is very close to that expected from the paraxial theory image vertical size $\Delta x_2 = 5$ μm. However, the whole image is curved to a parabolic shape. This happens due to Bragg reflections from the crystals in the dispersing element D_R (see [6,7] for details).
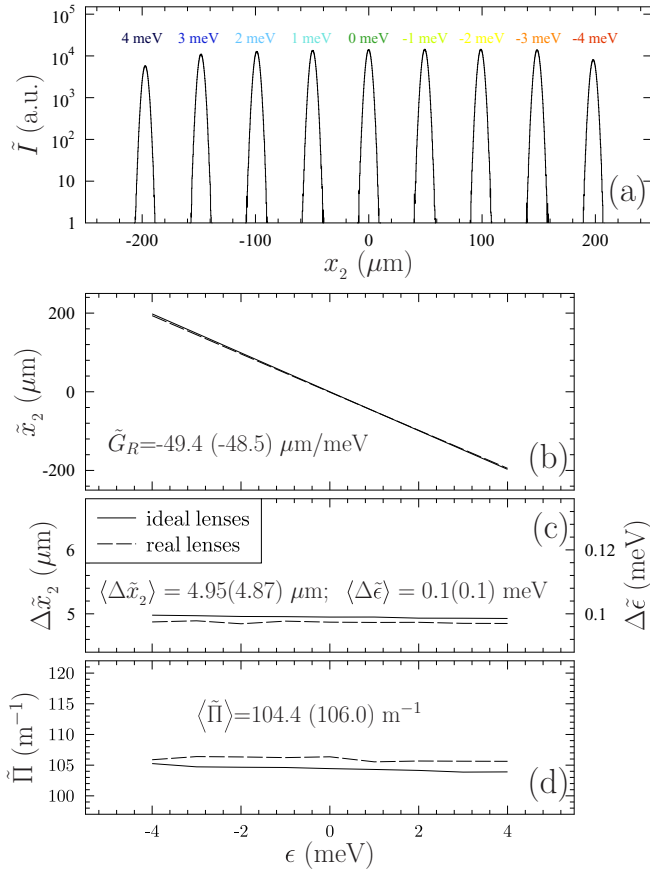
FIG. 6. Performance characteristics of the x-ray echo spectrometer with the refocusing system composed of ideal lenses or real CRLs as focusing elements. (a) Reduced image profiles calculated for various values of energy transfer ε in inelastic x-ray scattering under the same conditions as in Fig. 5. (b) Image peak position $\tilde{x}_2$, (c) reduced image size $\Delta\tilde{x}_2$, and (d) curvature $\tilde{\Pi}$ of the best-fit parabola to the image profile as a function of ε. Solid lines present results for the ideal lenses, while dashed lines and values in parentheses are for the real CRLs.

A 1D (strip) detector would measure a distribution shown in Fig. 5(b) with a vertical spread $\Delta\tilde{X} \simeq 32 \ \mu$m much larger than $\Delta x_2 = 5 \ \mu$m, and therefore would result in an asymmetric and much broadened instrumental spectral function. The detrimental effect of the curvature is significant only if the horizontal secondary source size is large, as in the case considered here of $\Delta Y_1 = 300 \ \mu$m.

The problem can be circumvented by using a 2D pixel detector and the following data evaluation [6]. The image in Fig. 5(a) is flattened by subtracting the best fit parabola $x_2 = \Pi y_2^2 + x_2(0)$ and integrating over y_2. The resulting reduced vertical profile, shown in Fig. 5(c), fits to a Gaussian function over an intensity range of at least four orders of magnitude with a width $\Delta\tilde{x}_2 = 4.95 \pm 0.02 \ \mu$m (FWHM), which is in very good agreement with the expected $\Delta x_2 = 5 \ \mu$m.

Further simulations show that this picture remains valid also in the case of inelastic x-ray scattering with nonzero energy transfer $\varepsilon \neq 0$. What changes is the position of the image, which shifts linearly with ε in the vertical direction along

x_2 with a linear dispersion rate $\tilde{G}_R = -49.4 \ \mu$m/meV [see Figs. 6(a) and 6(b)], in agreement with that predicted by the paraxial theory $G_R = -50 \ \mu$m/meV. The reduced image size and therefore the spectral resolution of the spectrometer are independent of ε [see Fig. 6(c)]. The results of Figs. 6(a)–6(c) confirm one of the key properties of x-ray echo spectrometers: their capability of imaging IXS spectra with high resolution and contrast.

Figure 6(d) demonstrates another important feature: the curvature $\tilde{\Pi}$ of the best-fit parabola to the image profile is practically independent of ε. This is in agreement with the theory [6], which predicts that $\Pi = UA_R/2f_2^2$, where $U = f_1(1 - b_2b_3)/|b_1b_2b_3| \cos\theta_2$, and therefore that Π is an invariant of the refocusing system, independent of the IXS energy transfer ε. Due to this, the curvature Π can be determined in practice from the elastic signal and applied to flatten numerically the inelastic signals, and thus to overcome degradation of the spectral function and resolution due to the large horizontal size of the secondary source. With the parameters of the spectrometer considered here we calculate $\Pi = 102 \ $m^{-1} and $\Delta X_2 = \Pi(\Delta Y f_2/2f_1)^2 = 31 \ \mu$m, which are close to $\tilde{\Pi} = 104.4 \ $m^{-1} and $\Delta\tilde{X} = 32 \ \mu$m calculated numerically for the ideal lenses [see Figs. 5(a) and 6(c)].

The picture does not change if realistic absorbing parabolic compound refractive lenses are used [9] instead of the ideal lens. The appropriate results of simulations are shown by dashed lines in Figs. 6(b)–6(d). The only major difference is in the signal strength, which is reduced by a factor of 41 (assuming $\Upsilon_v \times \Upsilon_h = 1.5 \times 1.5$-mrad^2 angular divergence of x rays from the source) because of the effective geometrical aperture reduced by photoabsorption.
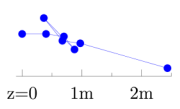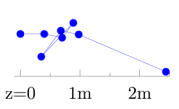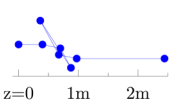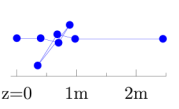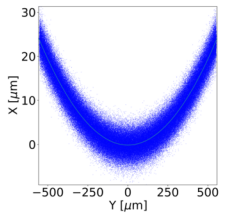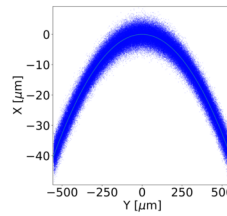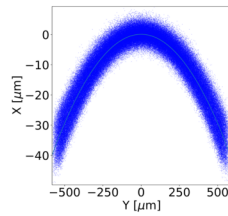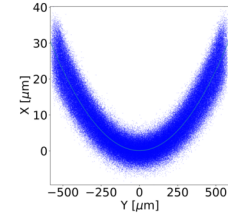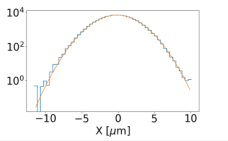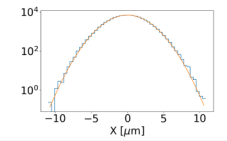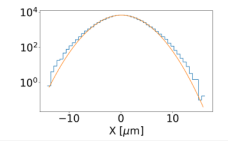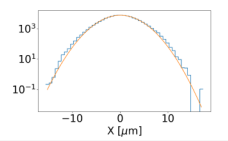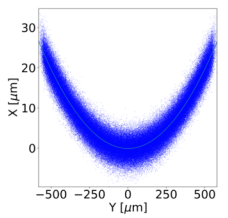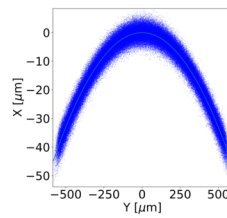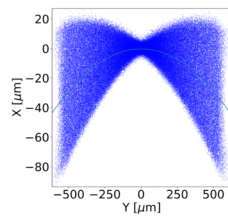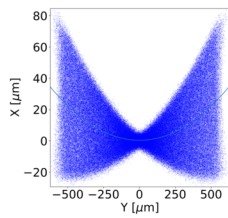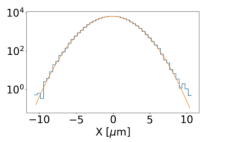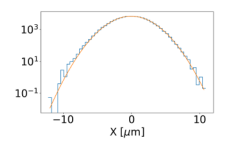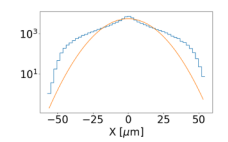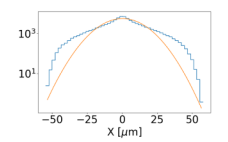
Here we conclude that the refocusing system composed of parabolic lenses represents an aberration-free imaging system capable of making sharp images of IXS spectra.

Focusing mirrors certainly may feature a significantly larger aperture; however, would they be also able to produce aberration-free IXS images?

IV. IXS IMAGING WITH MIRRORS

Unlike paraboloidal lenses, curved grazing incidence mirrors are in general not good x-ray imaging devices. Some particular combinations of two or more reflectors may comply with the Abbe sine condition and perform as good imaging systems. A prominent example is the Wolter-type mirror pairs [10,11]. The two mirrors that play the role of collimating and focusing elements in the refocusing system of the x-ray echo spectrometer with the dispersing system in between may perform similarly to a Wolter-type imaging system. In particular, a paraboloidal double-mirror system in a collimating-plus-focusing configuration has the great advantage of producing parallel x rays between the two reflections, which is perfect for the proper performance of a plane dispersive system ("diffraction grating") inserted in between [25]. The Abbe sine condition is perfectly fulfilled for the 1:1 1D-imaging case with no dispersing element in between [6]. However, the question still remains open whether perfect imaging can be achieved if a dispersing system is included, and whether this is valid in the 2D case, as x-ray echo spectrometers require.

TABLE II. Beam cross sections in image plane 2 calculated for the elastic-scattering case $\varepsilon = 0$ for the refocusing system of the x-ray echo spectrometer in four different mirror-crystal configurations with paraboloidal mirrors as collimating and focusing elements. Two cases of the angular apertures $\Upsilon_v \times \Upsilon_h$ are considered. Numerical values are provided for the vertical image size $\Delta \tilde{X}_2$ in image plane 2, reduced image size $\Delta \tilde{x}_2$, and the spectral resolution $\Delta \tilde{\varepsilon}$. The configuration graphs show side views of the beam trajectories (optical axes). The numbers in square brackets correspond to calculations with the horizontal angular aperture increased to $\Upsilon_h = 10$ mrad. The numbers highlighted in gray correspond to best imaging cases.

	I	II	III	IV
Configurations	$(-|\pi-, \pi-, \pi+, 0+|-)$ $G_D < 0$	$(-|\pi+, \pi+, \pi-, 0-|-)$ $G_D > 0$	$(-|\pi-, \pi-, \pi+, 0+|+)$ $G_D < 0$	$(-|\pi+, \pi+, \pi-, 0-|+)$ $G_D > 0$
$\Delta \tilde{X}_2$ [μm]	24.29±0.04 [26.9±0.1]	40.73±0.08 [45.03±0.2]	40.1±0.2 [44.0±0.6]	30.55±0.09 [34.1±0.5]
$\Delta \tilde{x}_2$ [μm]	5.28±0.01 [5.28±0.01]	5.43±0.01 [5.42 ±0.01]	7.58±0.02 [29.1±0.1]	7.56±0.01 [29.1±0.1]
$\Delta \tilde{\varepsilon}$ [μeV]	105.5±0.3 [105.5±0.3]	108.7±0.3 [108.4±0.2]	151.6±0.4 [583 ±2]	151.3±0.3 [583 ±2]

We study in this section IXS imaging with three different grazing incidence mirror systems composed of (i) two 2D paraboloidal mirrors [20], (ii) two KB systems [21] each formed by cylindric parabolic mirrors, and (iii) two Montel [22] systems, made as well of cylindric parabolic mirrors.
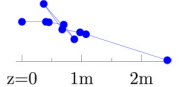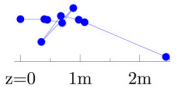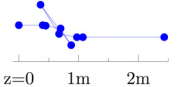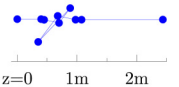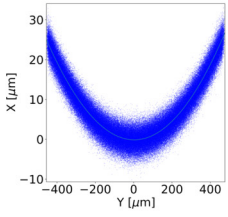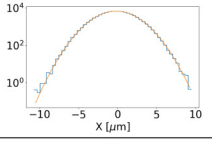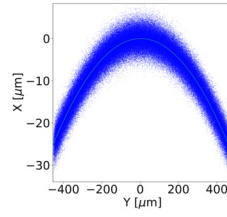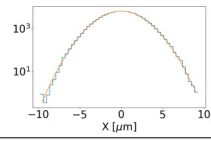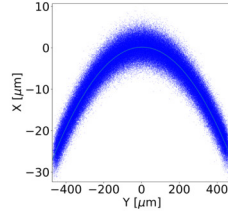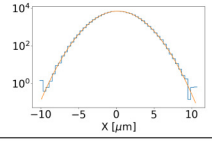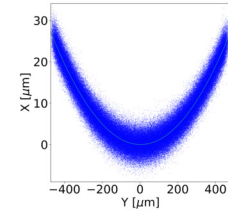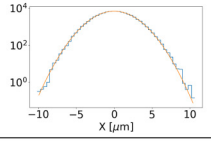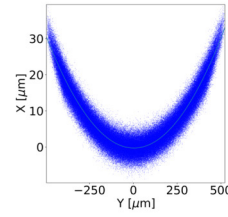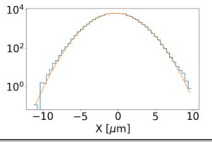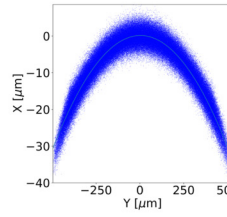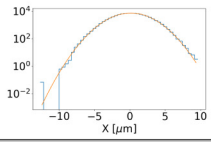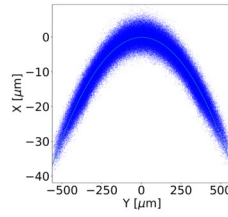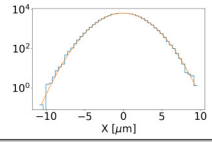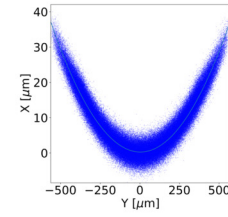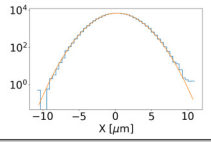
A. Elastic scattering $\varepsilon = 0$

We start with the refocusing system composed of two 2D paraboloidal mirrors and the CDDW dispersing element in between. The setting of the two paraboloids is not unique. They can be in a parallel or an antiparallel configuration. Extending the nomenclature used for crystal systems, we

can label these mirror configurations as $(-||+)$ and $(-||-)$, respectively. Here, plus and minus signs correspond to x-ray beams reflected counterclockwise and clockwise from an optical element, respectively. Importantly, the relative position of the CDDW system must be properly chosen to match the sign of the linear dispersion rate G_D on the sample in reference plane 1 [the first crystal may reflect counterclockwise (+) or clockwise (−)], which is critical to obeying the refocusing condition Eq. (1).

Table II shows graphs of four possible unique mirror-crystal configurations fulfilling the refocusing condition. Each configuration is coded by a sequence of signs. The left and right outer signs correspond to mirrors F_1 and F_2, respectively. The crystals are additionally characterized by the azimuthal

TABLE III. Similar to Table II, however with the results calculated for KB mirror systems as collimating and focusing elements.

	I	II	III	IV
Configurations	$z=0$ 1m 2m	$z=0$ 1m 2m	$z=0$ 1m 2m	$z=0$ 1m 2m
	$(-\|\pi-,\pi-,\pi+,0+\|-)$ $G_D < 0$	$(-\|\pi+,\pi+,\pi-,0-\|-)$ $G_D > 0$	$(-\|\pi-,\pi-,\pi+,0+\|+)$ $G_D < 0$	$(-\|\pi+,\pi+,\pi-,0-\|+)$ $G_D > 0$
$\Upsilon_v = 1.5$ mrad $\Upsilon_h = 1.5$ mrad				
$\Upsilon_v = 1.5$ mrad $\Upsilon_h = 10$ mrad				
$\Delta\tilde{X}_2$ [μm]	26.92±0.02 [33.32±0.02]	26.88±0.02 [33.18±0.02]	27.16±0.02 [36.77±0.02]	27.19±0.02 [36.88±0.03]
$\Delta\tilde{x}_2$ [μm]	5.11±0.01 [5.35±0.01]	5.11±0.01 [5.34 ±0.01]	5.13±0.01 [5.35 ±0.01]	5.13±0.01 [5.34 ±0.01]
$\Delta\tilde{\varepsilon}$ [μeV]	102.2±0.2 [107.0±0.2]	102.1±0.3 [106.8±0.3]	102.7±0.2 [107.0±0.1]	102.6±0.2 [106.8±0.2]

angles of incidence π or zero (see [1,6] for details). Configurations with all signs reversed including the G_D sign represent four equivalent configurations.

Table II presents results of the ray tracing simulations: the images and the reduced image profiles [similar to those in Figs. 5(a)–5(e)]. The simulations are performed for two different angular apertures: $\Upsilon_v = \Upsilon_h = 1.5$ mrad (the nominal case of the 0.07-nm^{-1} momentum-transfer resolution) and $\Upsilon_v = 1.5$ mrad, $\Upsilon_h = 10$ mrad (a larger horizontal aperture). Table II also provides calculated values of the vertical image size $\Delta\tilde{X}_2$, the reduced image size $\Delta\tilde{x}_2$, and the spectral resolution $\Delta\tilde{\varepsilon}$.

Only the $(-\|\|-)$ mirror configurations I and II result in sharp reduced images with Gaussian profiles and image sizes of $\Delta\tilde{x}_2 \simeq 5$ μm in agreement with those expected from the paraxial theory value of $\Delta x_2 = 5$ μm, both for $\Upsilon_h = 1.5$ and 10 mrad. The imaging properties of systems III and IV are worse but still almost as good for $\Upsilon_h = 1.5$ mrad. However, major aberrations explode with increasing the horizontal

angular aperture to 10 mrad. According to Table II results, configuration I is the best, providing the smallest image size $\Delta\tilde{X}_2$, the smallest reduced image size $\Delta\tilde{x}_2$, and therefore the best spectral resolution $\Delta\tilde{\varepsilon}$, in agreement with the design value and with the lens case.

Table III shows results of similar calculations for the refocusing system, in which the two paraboloidal mirrors are replaced by two KB mirror systems. The vertical focusing mirrors (VFMs) are placed as the paraboloidal mirrors at distances f_1 and f_2 from reference planes 1 and 2, respectively, while the horizontal focusing mirrors (HFMs) are at 50 and 100 mm downstream of the VFMs, respectively, with the focal lengths of the HFMs appropriately corrected. Remarkably, the refocusing system composed of the KB mirror systems produces sharp images in all four possible configurations (as the paraboloidal mirrors in the best configuration I).

The refocusing system comprising Montel mirrors performs in all four possible configurations very similar to the KB mirror case, provided the $\Upsilon_h = 1.5$-mrad angular aperture

TABLE IV. Reduced vertical image size $\Delta \tilde{x}_2$ (in μm) in reference plane 2 as a function of Υ_v (with a fixed $\Upsilon_h = 1.5$ mrad) calculated for paraboloidal, KB, and Montel mirror systems in configuration I. Values are shown for the elastic-scattering case ($\varepsilon = 0$) and for the inelastic case $\varepsilon = 4$ meV in brackets (see Sec. IV B 2 for details). Note that $\Delta \tilde{x}_2 = 5$ μm corresponds to a spectral resolution of $\Delta \varepsilon = 0.1$ meV.

Υ_v (mrad)	Paraboloids	KBs	Montel
1.5	5.3 (5.4)	5.1 (5.1)	5.7 (5.5)
3.0	6.0 (6.5)	5.5 (5.5)	6.9 (6.5)
6.0	7.8 (8.8)	6.6 (6.6)	9.8 (8.6)
12.0	11.3 (13.8)	9.1 (9.1)	15.1 (13.2)
24.0	18.6 (26.3)	13.8 (14.3)	

case is considered (see Table VII of Appendix B). However, the Montel mirrors are more sensitive to the horizontal divergence, producing significantly worse results in the $\Upsilon_h = 10$-mrad angular aperture case especially in configurations I and IV. The better performance of the KB mirror system compared to the Montel mirror system may be due to the fact
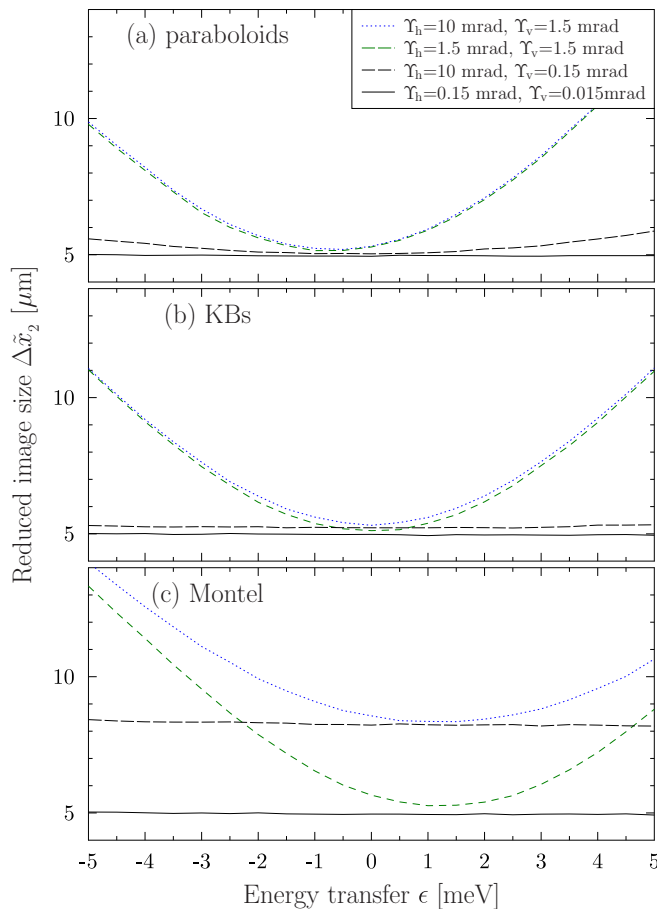

FIG. 7. Reduced vertical image size $\Delta \tilde{x}_2$ in reference plane 2 as a function of the energy transfer ε, calculated for the refocusing system with (a) paraboloidal mirrors, (b) KB mirror systems, and (c) Montel systems, all in configuration I (see Table II) for different values of the angular apertures Υ_h and Υ_v.

that the VFMs and HFMs in the KB case are perfectly aligned along the optical axis (x-ray trajectory). In contrast, VFMs and HFMs are orthogonal to each other in the Montel case, composing a system with an ill-defined optical axis.

The performance of the refocusing systems composed of KB mirrors appears to be also least sensitive to increasing the vertical angular aperture Υ_v, as the results of the calculations of the reduced image size $\Delta \tilde{x}_2$ and of the spectral resolution $\Delta \varepsilon$ show, presented in Table IV. The image size and spectral resolution degrade roughly by a factor of 2 from $\Delta \varepsilon = 0.1$ to $\simeq 0.2$ meV with increasing Υ_v from the nominal 1.5 mrad to 10 mrad. Note that the calculations are performed with mirrors and crystals long enough to accept the full beam.

In summary, in the elastic-scattering case, the refocusing systems composed of focusing mirrors perform in the best mirror-crystal configurations very similarly to the systems composed of lenses. Whether this is still true for the inelastic-scattering case is a question we study in the next section.

B. Inelastic scattering $\varepsilon \neq 0$

1. Aberrations in the image plane

In the case of lenses, the reduced image size in reference plane 2 does not change if inelastic scattering ($\varepsilon \neq 0$) takes place. This is no longer the case if mirrors are used instead of lenses. Indeed, the reduced image size in reference plane 2 plotted versus ε in Fig. 7 appears to grow quadratically with ε: $\Delta \tilde{x}_2(\varepsilon) - \Delta \tilde{x}_2(0) \propto \varepsilon^2$. Thus the mirror systems behave very differently compared to the lens systems: the spectral resolution degrades with $|\varepsilon|$. This degradation can be reduced or even eliminated if the vertical angular aperture Υ_v is diminished substantially by a factor 10 or 100. This, however, would reduce the photon flux in the detector to unacceptably low values. Interestingly, the horizontal angular aperture does not have the same effect, except for Montel mirror systems, which are very sensitive to large Υ_h.

The different behavior of the mirror- and lens-based systems could be related to focusing element F_2, while collimating element F_1 functions in the same way both in the elastic- and inelastic-scattering regimes [see Figs. 1(v_e)–1(v_i)]. In contrast, it is not the case for focusing element F_2, as the incidence angle changes with ε for it. This is probably of no significance if lenses are used as F_2, for which the incidence angle is close to normal. This appears to be important if grazing incidence mirrors are used instead. However, the studies, which are discussed in Appendix B and in Fig. 13, show that no optimal f_2 value can be found in any of the considered mirror cases, which would eliminate or mitigate the degradation of the spectral resolution with ε. They show, though, that the 1:1 imaging is preferred to be least sensitive to spectral resolutions degradation by large angular apertures Υ_h and Υ_v.

2. Defocus correction in an oblique image plane

In this section we show that the degradation of the reduced vertical size when passing from elastic ($\varepsilon = 0$) to inelastic ($\varepsilon \neq 0$) scattering is merely the defocus aberration that can be easily compensated.
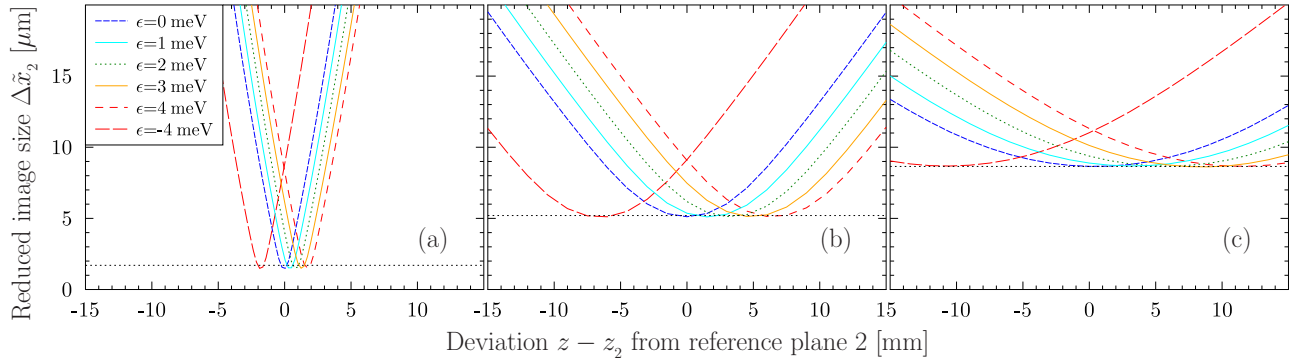
FIG. 8. Reduced vertical image size $\Delta\tilde{x}_2$ as a function of deviation $z - z_2$ from reference image plane 2, calculated for different energy-transfer values ε and for selected focal length values f_2 of imaging mirror F_2: (a) $f_2 = 0.4$ m, (b) $f_2 = 1.471$ m, and (c) $f_2 = 2.5$ m. Calculations are for the KB mirrors case in mirror-crystal configuration I (see Table III), and for the angular apertures $\Upsilon_h = \Upsilon_v = 1.5$ mrad. See Fig. 14 of Appendix B for similar results of the paraboloidal or Montel mirror systems.

For this, we calculate how the reduced image size changes along the optical axis for different values of ε. The results presented in Fig. 8 show that the smallest reduced image size (waist) for any ε is in fact equal to the elastic image size $\Delta\tilde{x}_2(\varepsilon = 0)$. However, it is attained with a shift $z_2(\varepsilon) - z_2(0)$ along the optical axis from the location z_2 of the nominal image plane.[2] The waist size scales with the focal length f_2 in Figs. 8(a)–8(c), because it changes the magnification factor $A_R = -b_{\cup_R} f_2 / f_1$, Eq. (5).

The waist position shifts linearly with ε as $z_2(\varepsilon) - z_2(0) = \varepsilon/\gamma$ (see Fig. 9). The slope γ depends on focal length f_2 of mirror F_2 and on mirrors' incidence angle φ, as illustrated in Figs. 9(a) and 9(b), respectively. The slope γ is independent of the CDDW-to-F_2 distance (the results of calculations are not shown).

The loci of the waists is therefore a line inclined to the optical z axis by an angle $\psi = G_R\gamma$. In particular, if $f_2 = 1.471$ m, which corresponds to the 1:1 imaging, the inclination of the IXS image plane is $\psi \simeq \varphi$ [see numerical values in the inset of Fig. 9(b)]. In a more general case, ψ is still proportional to φ but scales with the magnification factor of the refocusing system as $\psi \simeq \varphi (b_{\cup_R} f_2 / f_1)$ [see values in the inset of Fig. 9(a)].

The spectral resolution degradation in the nominal image plane 2 (see Fig. 7), therefore, can be compensated by inclination of the x-ray pixel detector by the angle ψ. Such an inclination may simultaneously improve the detector's spatial resolution.[3] For example, if the detector has a pixel size $p = 50$ μm, its projection on reference plane 2 and thus the

spatial resolution become $p\psi \simeq 1.5$ μm (for $\psi = 30$ mrad) or $p\psi \simeq 1.3$ μm (for $\psi = 25$ mrad).[4]

Figure 10 summarizes IXS imaging properties of the refocusing system composed of grazing incidence curved KB mirror systems and the pixel x-ray detector in the oblique image plane. The properties are very similar to those of the system composed of paraboloidal lenses. The only difference is that the aberration-free imaging takes place in the oblique image plane at the angle ψ to the optical axis. The imaging properties of the refocusing system composed of the paraboloidal or Montel mirror systems are very similar and presented in Fig. 14 of Appendix B. A slightly better resolution is found for KBs than for paraboloids and Montel systems.

C. Effect of glancing angle of incidence

Typically, the imaging property of a solitary mirror degrades with decreasing glancing angle of incidence because of the illumination of an increasing part of the optic. Here we study the effect of glancing angle of incidence φ on the imaging properties of the refocusing system composed of mirror pairs and the CDDW dispersing element in between.

Table V presents results of calculations of the image size in case of KB and paraboloidal systems for selected values of φ. They show that the image size slightly increases and therefore the spectrometer resolution degrades when glancing angle decreases. The output intensity remains constant if mirrors are used long enough to accept the whole beam (data not shown). This means that larger φ values are preferred. However, other considerations speak against large φ. Larger

---

[2]At the first glance, the beam size dependences in Fig. 8 may produce an impression that the vertical beam size changes with z as

$$\Delta\tilde{x}_2(z, \varepsilon) = \Delta\tilde{x}_2(0) \sqrt{1 + \{[z - z_2(\varepsilon)]/z_R\}^2} \qquad (9)$$

for any ε, i.e., as the Gaussian beam size would change with a waist size of $\Delta\tilde{x}_2(0)$ and Rayleigh range z_R [26,27]. However, this is not the case, because numerical simulations reveal a quadratic component at large z.

[3]A similar approach is used in soft-x-ray grating spectrometers (see, e.g., [28]).

[4]To be practical, the application of a high-Z sensor material is required with a photoabsorption length $L_a \ll p$. A CdTe 50×50-μm^2 pixel detector would be most optimal for this application. CdTe: $L_a = 6.5$ μm for 9.1-keV photons, $L_a = 11.4$ μm for 11.210-keV photons, $L_a = 22.9$ μm for 14.41-keV photons. To image a beam with a 400-μm large vertical size (corresponds to a 8-meV spectral window of imaging), a 12.5-mm CdTe sensor would be required. Photon-counting pixel detectors with such senors are state of the art [29].
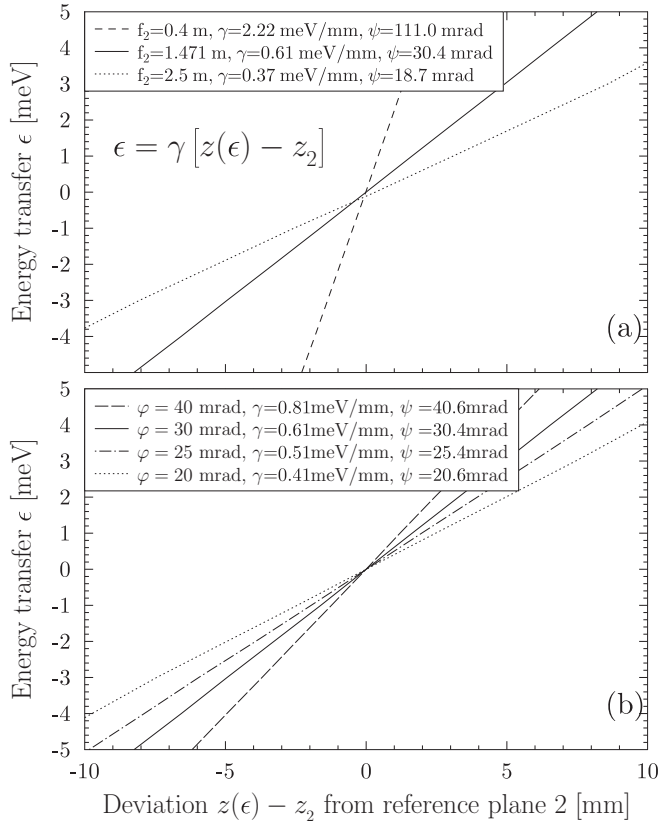
FIG. 9. Correspondence between the energy transfer ε and the deviation $z(\varepsilon) - z_2$ from reference plane 2 of the reduced image with the smallest size (waist). Calculated for the KB mirrors case. (a) Derived from data in Fig. 8 for selected focal length values f_2. Mirrors' incidence angle is $\varphi = 30$ mrad, and angular apertures $\Upsilon_v = \Upsilon_h = 1.5$ mrad. (b) Calculated with $f_2 = 1.471$ m (1:1 imaging) and selected values of glancing angle of incidence φ. See Fig. 15 of Appendix B for the results of the paraboloidal or Montel mirror systems.

φ requires multilayer coatings with smaller periods and eventually smaller reflectivity. Glancing angle of incidence $\varphi \simeq 30$ mrad is optimal for present-day technology and is therefore used in the current simulations.

D. Effect of slope errors

Mirrors' slope errors will surely contribute to broadening the reduced image size and degrading the spectrometer's spectral resolution. It is therefore important to determine the admissible values for the slope errors.

TABLE V. Reduced image size (in μm) in the refocusing system of the x-ray echo spectrometer comprising mirror systems with different glancing angles of incidence φ.

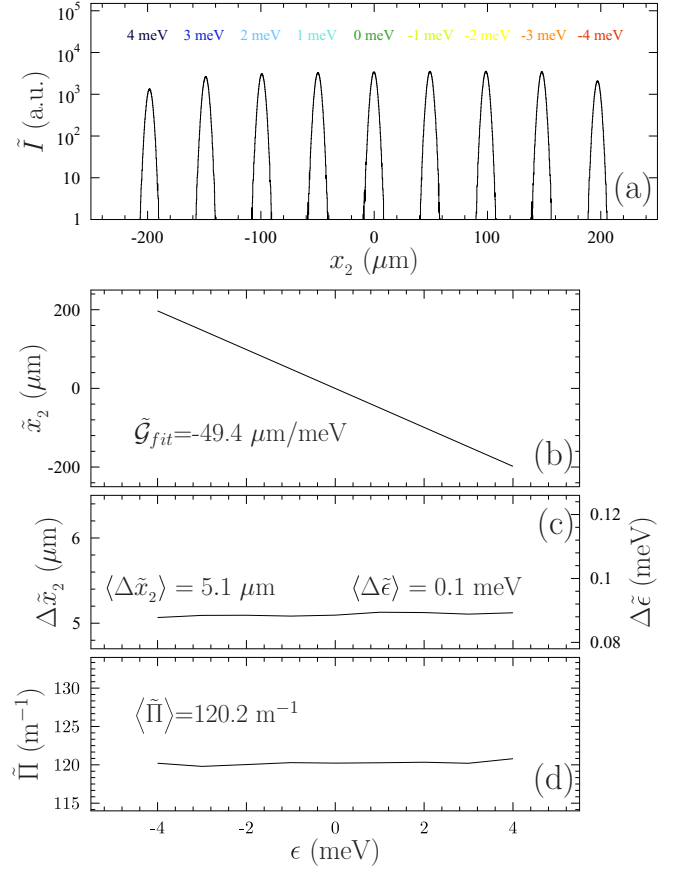| Mirror type/φ (mrad)	20	25	30	40
KB	5.29	5.17	5.10	5.05
Paraboloids	5.54	5.38	5.27	5.15

FIG. 10. Performance characteristics of the x-ray echo spectrometer with the refocusing system composed of KB mirrors. IXS spectra are imaged on the oblique image plane. Compare with the results of Fig. 6 presented for the case of lenses as the focusing elements, and with the results for the paraboloidal or Montel mirror systems in Fig. 16 of Appendix B.

Figure 11 presents results of the ray tracing calculations for reduced image profiles by the refocusing system composed of paraboloidal mirror pairs for selected values of slope errors: 0, 0.5, 1, and 2.5 μrad (rms), same for both mirrors. They show a rapid degradation of the reduced image size and signal strength with increasing slope errors, and indicate that the slope errors of the mirrors must stay below 0.5 μrad in the present case.

These results can be supported and understood by simple analytical considerations,[5] which in particular show that it is mirror F_2 with the largest focal length f_2 that is the critical

[5] Slope error ξ of a mirror with a focal length f results in additional relative broadening $\mu = 2\xi f/\Delta x$ of the image size Δx. For the resultant image size $\Delta x \sqrt{1 + \mu^2}$ to be not increased by more than 10%, the relative broadening should be $\mu \lesssim \sqrt{0.2} = 0.46$ and the slope errors $\xi \lesssim \mu \Delta x/2f$. Assuming $\Delta x = 5$ μm (FWHM) or $\Delta x = 2.13$ μm (rms), we obtain $\xi_1 \lesssim 1.2$ μrad (rms) for a mirror with $f_1 = 0.4$ m and $\xi_2 \lesssim 0.33$ μrad (rms) for a mirror with $f_2 = 1.471$ m. If a 20% broadening is admissible, then $m = 0.66$, and the corresponding admissible slope errors are $\xi_1 \lesssim 1.76$ μrad (rms) and $\xi_2 \lesssim 0.5$ μrad (rms).
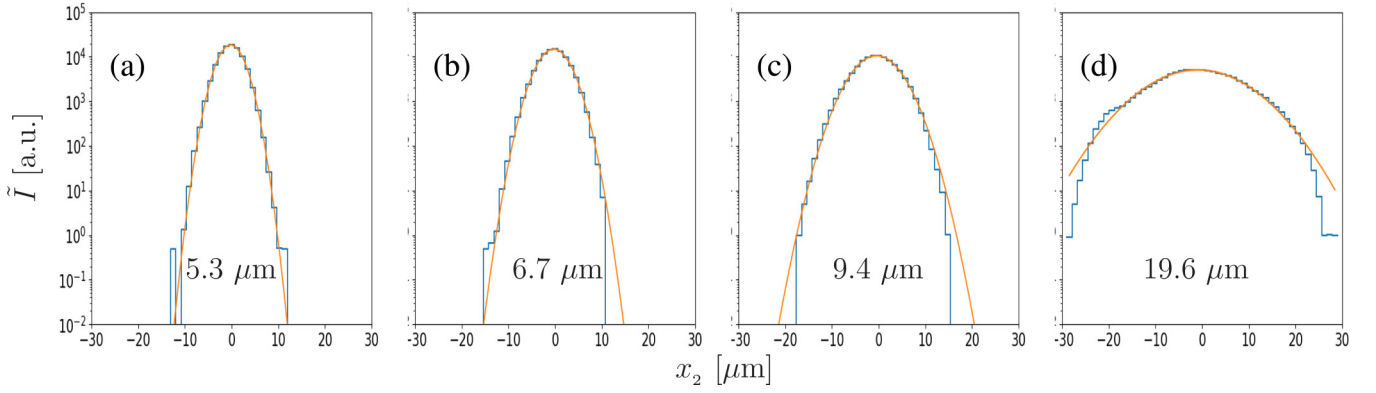
FIG. 11. Reduced image profiles in elastic scattering ($\varepsilon = 0$) for paraboloidal mirrors with different slope errors: (a) 0, (b) 0.5, (c) 1.0, and (d) 2.5 μrad (rms), respectively. The corresponding image size widths $\Delta \tilde{x}_2$ (FWHM) are displayed in the graphs.

optic requiring such a small slope error value. Therefore, using mirrors with smaller focal lengths is preferable from this point of view.

V. IMAGING IXS SPECTRA OF "GLYCEROL"

Finally, in this section we study the ability of the x-ray echo spectrometer to image IXS spectra of real samples. As an example, we select a liquid sample with properties closely resembling glycerol at room temperature.

The IXS spectra in liquids are typically modeled by the normalized dynamical structure factor

$$\frac{S(Q, \varepsilon)}{S(Q)} = f_\varrho \delta(\varepsilon) + \frac{1 - f_\varrho}{\pi} \frac{\Gamma_\varrho \Omega_\varrho^2}{\left(\varepsilon^2 - \Omega_\varrho^2\right)^2 + \varepsilon^2 \Gamma_\varrho^2}, \quad (10)$$

$$\Omega_\varrho = v_s \hbar Q, \quad \Gamma_\varrho = BQ^2, \quad (11)$$

which is a sum of the delta function for the elastic component and the damped harmonic oscillator for the inelastic component measured at selected momentum transfer Q [30]. The sound velocity $v_s = 2.8$ km/s, reduced broadening $B = 3$ nm^2 meV, and elastic line fraction $f_\varrho = 0.7$ are assumed to be constant for simplicity, i.e., Q independent, which is in fact not necessarily the case in practice. This assumption represents merely an interpolation of the known data for glycerol liquid [31,32] into the yet unexplored range of $Q \lesssim 0.5$ nm^{-1}. The graphs in the lower row of Fig. 12 show in red (solid line) the normalized dynamical structure factor $S(Q, \varepsilon)/S(Q)$ of the "glycerol" calculated for selected Q values using Eqs. (10) and (11). The elastic line in green (dashed line) is a Gaussian with FWHM of 0.1 meV—equivalent to the resolution function of the x-ray echo spectrometer.
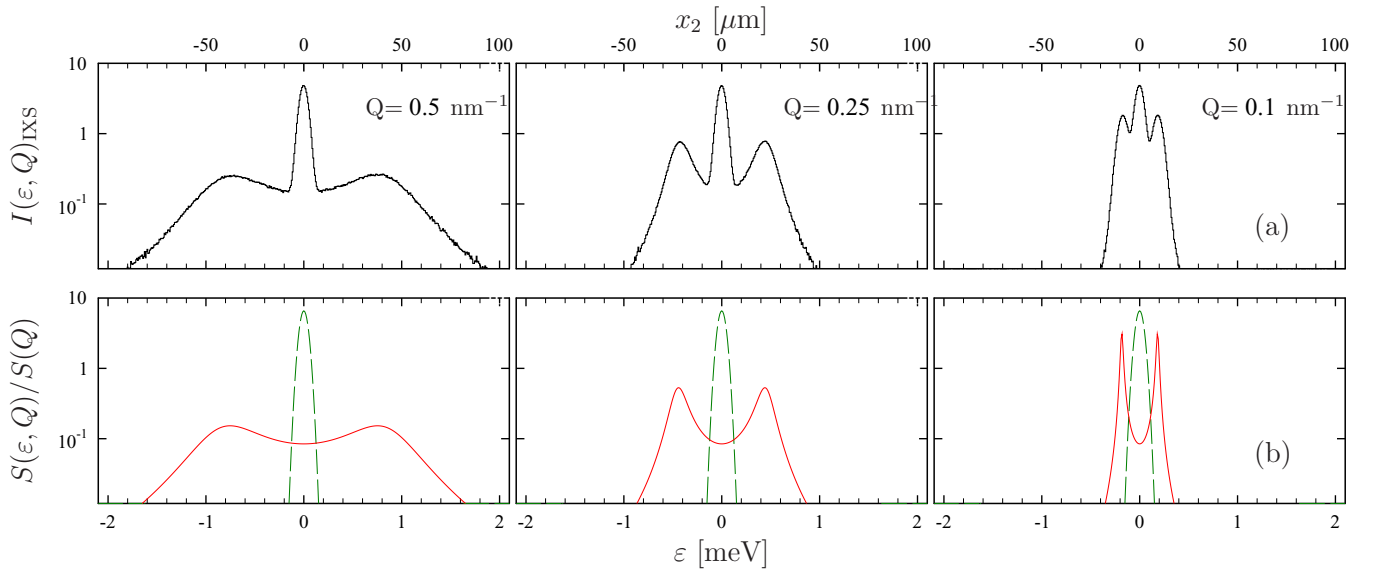

FIG. 12. IXS spectra of "glycerol" liquid at selected momentum-transfer values Q. Upper row: IXS spectra $I(\varepsilon, Q)_{\text{IXS}}$ obtained by ray tracing though the refocusing system of the 0.1-meV-resolution x-ray echo spectrometer composed of ideal lenses. The system with paraboloidal mirrors produces almost identical results provided the IXS spectra are imaged on the oblique plane. Lower row: The normalized dynamical structure factor $S(\varepsilon, Q)/S(Q)$ used in the ray tracing simulations is calculated with Eqs. (10) and (11) and is shown by the red solid line. The elastic line in green (dashed line) is a Gaussian with FWHM of 0.1 meV—equivalent to the resolution function of the x-ray echo spectrometer.

In the simulations presented in the previous sections, the sample introduced a constant energy transfer ε ($\varepsilon = 0$ for the elastic case and $\varepsilon \neq 0$ for the inelastic case). Now, each ray will be affected by a random ε sampled by $S(Q, \varepsilon)/S(Q)$, thus simulating the real effect of the photon energy change by the sample with a probability determined by the ideal IXS spectrum of Eq. (10).

The real IXS spectra measured in experiments represent a convolution of $S(Q, \varepsilon)/S(Q)$ with the instrumental function. This convolution is naturally included in the ray tracing simulations. The graphs in the upper row of Fig. 12 present the glycerol IXS spectra obtained by the ray tracing through the refocusing system of the x-ray echo spectrometer equipped with the ideal lenses. The system equipped with the paraboloidal mirrors produces almost identical results (not shown). However, in the latter case, the detector plane has to be inclined by an angle of $\varphi = 30.5$ mrad with the optical axis. Recall that the spatial image produced in the detector is reduced by removing the parabola calculated for the elastic scattering with parameters provided in Fig. 6 for the lenses and in Fig. 10 for KB mirror systems.

The ray tracing results practically reproduce the spectral features of $S(Q, \varepsilon)/S(Q)$ for $Q = 0.5$ and 0.25 nm^{-1}. The phonon peaks are also well resolved in the $Q = 0.1$-nm^{-1} case, however, they appear blurred because the phonon lines are already narrower than the resolution function. The example of the presented simulations confirms that x-ray echo spectrometers are capable of aberration-free imaging IXS spectra.

VI. CONCLUSIONS

We have studied conditions for aberration-free imaging of IXS spectra with x-ray echo spectrometers. Aberration-free imaging is essential for achieving high-resolution high-contrast instrumental functions. Numerical ray tracing was applied to a particular case of a 0.1-meV-resolution echo-type IXS spectrometer operating with 9-keV x rays.

X rays from a Gaussian polychromatic source being dispersed and therefore defocused on the scattering sample by the defocusing system are refocused in the image plane of the refocusing system into a sharp image. The image shifts transversely in the dispersion plane by an amount proportional to inelastic-scattering energy transfer ε, thus ensuring imaging of IXS spectra.

The images are laterally curved. However, the curvature is spectrometer invariant, determined by the parameters of the Bragg reflecting crystals of the dispersing element and the focal distances of the focusing elements. The curved images of all elastic and inelastic components can therefore be reduced to flat images. The reduced images reveal Gaussian profiles, if flawless optical elements are in use.

We show that all ε components of IXS spectra are imaged aberration free, featuring Gaussian profiles of constant width, provided the collimating and focusing optics of the refocusing system of the x-ray echo spectrometer are composed of lenses.

If curved grazing incidence mirror systems are used instead (paraboloidal, parabolic KB, or parabolic Montel), the images

of all ε components still can be Gaussian and sharp when recorded on the detector plane tilted with respect to the optical axis. The inclination of this oblique image plane to the optical axis is equal to the grazing angle of incidence, in the case of 1:1 imaging by the refocusing system. Compensation of the defocus aberration by inclining the x-ray imaging pixel detector simultaneously improves the detector's spatial resolution.

The refocusing system of the 0.1-meV-resolution x-ray echo spectrometer may feature sharp aberration-free images of IXS spectra using any considered mirror type assuming the angular aperture is $\Upsilon_v = \Upsilon_h = 1.5$ mrad (required by the spectrometer's nominal momentum-transfer resolution $\Delta Q = 0.07$ nm^{-1}). However, the KB and Montel mirror systems provide sharp images both in the $(-||-)$ and $(-||+)$ mirror configurations, while the paraboloidal mirrors work properly only in the $(-||-)$ configuration. KB mirror systems appear to be the best imaging devices, as the high image quality by the KB systems is preserved in all configurations also with the horizontal angular aperture increased to $\Upsilon_h = 10$ mrad. The paraboloidal mirrors can perform similarly, however, only in the 1:1 imaging case in the $(-||-)$ configuration. The performance of the KB mirror systems is also least sensitive to the vertical angular aperture Υ_v.

The instrumental function of echo-type IXS spectrometers has sharp high-contrast Gaussian tails. This is a great advantage over the long Lorentzian tails of the instrumental functions of present-day narrow-band scanning IXS spectrometers [5]. In practice, the contrast of the instrumental function will rely on the quality (smallness of the slope errors) of the mirrors of the x-ray echo spectrometers. The simulations show that slope errors better that 0.5 μrad are critical to avoid instrumental function degradation in the 30-mrad grazing incidence mirror case (Fig. 11) with a focal length of $f_2 = 1.4$ m.

Initial design parameters of the x-ray echo spectrometer derived by analytical ray-tracing theory [6] are in very good agreement with the results of the numerical simulations. In particular, no meaningful change in the resolution is observed if all the crystals are put at the same position, as the analytical theory assumes.

The results of the studies are applicable also to hard-x-ray imaging spectrographs [16], which represent a subsystem of x-ray echo spectrometers. The spectrographs, unlike x-ray echo spectrometers, are dealing with imaging IXS spectra with a tight nondispersed monochromatic secondary source on the sample.

The range of applications of the echo-type IXS spectrometers and IXS spectrographs of course includes resonant IXS [33], as a particular case.

APPENDIX A: MULTICRYSTAL DISPERSING ELEMENTS

The optical schemes and the spectral transmission functions of the four-crystal dispersing elements of the defocusing and of the refocusing systems are presented in Figs. 2 and 3, respectively. In this section we provide Table VI with the parameters of the crystals for both systems.

APPENDIX B: IXS IMAGING PERFORMANCE WITH DIFFERENT MIRROR SYSTEMS

Very often the results of the calculations of imaging IXS spectra with different types of mirror systems look similar. Not to overwhelm the main part of the paper with too many details we have moved such data into this Appendix, which contains a collection of supplementary tables and figures.

Table VII shows elastic signal imaging with the Montel mirror systems, similar to those shown for the paraboloidal and KB mirror systems in Tables II and III, respectively.

To gain more insight into the problem of spectral resolution degradation in mirror systems with ε (Sec. IV B 1), we study

the reduced image size dependence on the focal length f_2. The results are shown in Fig. 13. If the angular aperture of the system is relatively small ($\Upsilon_v = \Upsilon_h = 1.5$ mrad, solid lines), the reduced sizes for both the elastic ($\varepsilon = 0$, blue) and inelastic ($\varepsilon = 4$ meV, green) images change almost linearly with f_2. In the large-f_2 range, the elastic lines (blue) approach the reference case of imaging with ideal lenses (red lines). The inclination is defined by the magnification factor of the refocusing system $b_{\cup_R} f_2 / f_1$. If the horizontal acceptance is increased to $\Upsilon_h = 10$ mrad (dashed lines), the result does not change much for the KB mirrors [see Fig. 13(b)]. However, in the case of the paraboloids [see Fig. 13(a)], the linear behavior breaks down and the reduced image size increases dramatically, albeit with one exception. For $f_2 = 1.471$ m, which corresponds to the 1:1 imaging case, the image sizes are exactly the same as for the small angular aperture case (solid lines). This is probably related to the fact that the Abbe sine condition for two parabolic mirrors is perfectly fulfilled in the 1:1 imaging case [6]. Montel systems perform similarly to KB systems; however, the image size increases quickly with increases in the horizontal angular aperture.
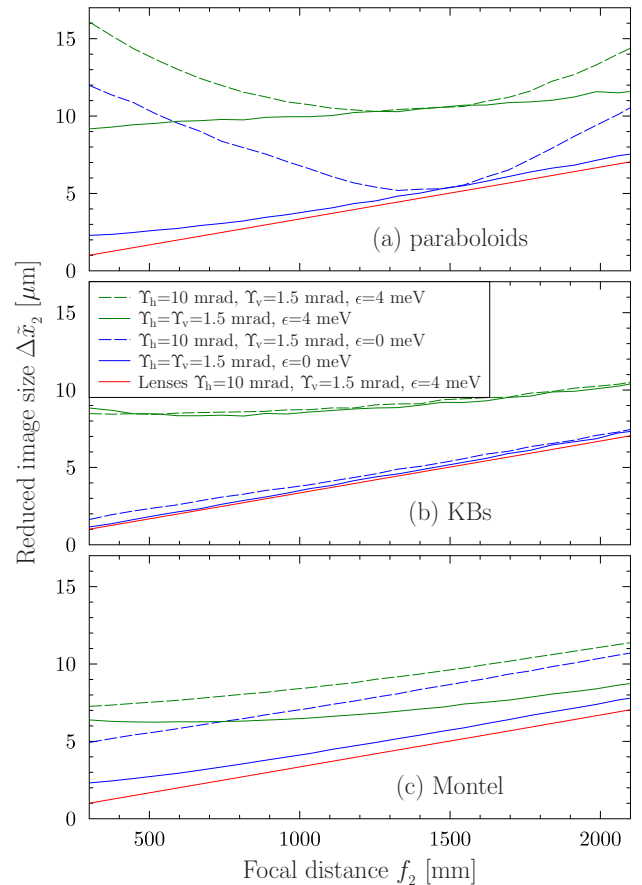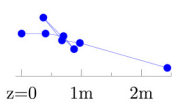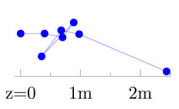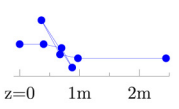
TABLE VI. Parameters of the CDDW-type in-line crystal optics designed as dispersing elements D_D and D_R of the defocusing $\hat{O}_D$ and refocusing $\hat{O}_R$ systems of the 0.1-meV-resolution x-ray echo spectrometer. For each optic, the table presents crystal elements ($e =$ C, D_1, D_2, W) and their Bragg reflection parameters: (hkl), Miller indices of the Bragg diffraction vector $\boldsymbol{H}_e$; η_e, asymmetry angle; θ_e, glancing angle of incidence; Bragg reflection intrinsic spectral width $\Delta E_e^{(s)}$ and angular acceptance $\Delta \theta_e^{(s)}$ in symmetric scattering geometry, respectively; b_e, asymmetry ratio; and $s_e \mathcal{D}_e$, angular dispersion rate with deflection sign. For each optic, also shown are angular acceptance $\Delta \theta_X$ ($X = D, R$) and spectral bandwidth ΔE_X as derived from the dynamical theory calculations, the angular spread of the dispersion fan $\Delta \theta'_X = |\mathcal{D}_{\cup_X}| \Delta E_X$, and the cumulative values of the asymmetry parameter $b_{\cup_X}$ and the dispersion rate $\mathcal{D}_{\cup_X}$. X-ray photon energy is $E = 9.13708$ keV.

Crystal element (e) [material]	$\boldsymbol{H}_e$ (hkl)	η_e (deg)	θ_e (deg)	$\Delta E_e^{(s)}$ (meV)	$\Delta \theta_e^{(s)}$ (μrad)	b_e	$s_e \mathcal{D}_e$ ($\frac{\mu\text{rad}}{\text{meV}}$)
D_D: CDDW ($\pi+, 0-, 0+, 0-$), Fig. 2							
1 C [Si]	(1 1 1)	−10.5	12.5	1304	32	−0.09	−0.02
2 D_1 [Si]	(8 0 0)	77.7	88	27	85	−1.38	−1.19
3 D_2 [Si]	(8 0 0)	77.7	88	27	85	−1.38	+1.19
4 W [Si]	(1 1 1)	10.5	12.5	3013	71	−11.2	−0.24
Cumulative values		$\Delta \theta_D$ (μrad)	ΔE_D (meV)	$\Delta \theta'_D$ (μrad)	$b_{\cup_D}$		$\mathcal{D}_{\cup_D}$ ($\frac{\mu\text{rad}}{\text{meV}}$)
		57	3.5	112	1.91		−31.7
D_R: CDDW ($\pi+, \pi+, \pi-, 0-$), Fig. 3							
1 C [Ge]	(1 1 1)	−10.5	12.0	3013	71	−0.07	−0.02
2 D_1 [Si]	(8 0 0)	−83.75	88	27	85	−0.52	−1.50
3 D_2 [Si]	(8 0 0)	−83.75	88	27	85	−0.52	+1.50
4 W [Ge]	(1 1 1)	10.5	12.0	3013	71	−14.75	−0.31
Cumulative values		$\Delta \theta_R$ (μrad)	ΔE_R (meV)	$\Delta \theta'_R$ (μrad)	$b_{\cup_R}$		$\mathcal{D}_{\cup_R}$ ($\frac{\mu\text{rad}}{\text{meV}}$)
		262	8	272	0.27		−34.15

FIG. 13. Reduced image size in image plane 2 vs focal distance f_2 of the imaging optical systems F_2 calculated for the refocusin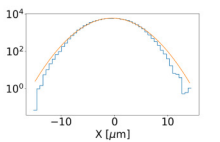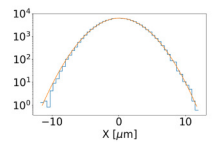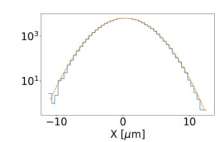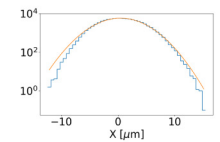g system with (a) the paraboloidal mirrors, (b) KB mirror systems, and (c) Montel systems, all in configuration I (see Tables II and III) for different values of the angular apertures Υ_h and Υ_v. Red lines show results of calculations for the ideal lens case, as a reference.

TABLE VII. Beam cross sections in image plane 2 calculated for the elastic-scattering case $\varepsilon = 0$ for the refocusing system of the x-ray echo spectrometer in four different mirror-crystal configurations with Montel mirror systems as collimating and focusing elements. Two cases of the angular apertures $\Upsilon_v \times \Upsilon_h$ are considered. Numerical values are provided for the vertical image size $\Delta \tilde{X}_2$ in image plane 2, reduced image size $\Delta \tilde{x}_2$, and spectral resolution $\Delta \tilde{\varepsilon}$. The configuration graphs show side views of the beam trajectories (optical axes). The numbers in the square brackets correspond to calculations with the horizontal angular aperture increased to $\Upsilon_h = 10$ mrad. The numbers highlighted in gray correspond to best imaging cases.

	I	II	III	IV
Configurations	$(-|\pi-, \pi-, \pi+, 0+|-)$ $G_D < 0$	$(-|\pi+, \pi+, \pi-, 0-|-)$ $G_D > 0$	$(-|\pi-, \pi-, \pi+, 0+|+)$ $G_D < 0$	$(-|\pi+, \pi+, \pi-, 0-|+)$ $G_D > 0$
$\Upsilon_v = 1.5$ mrad $\Upsilon_h = 1.5$ mrad				
$\Upsilon_v = 1.5$ mrad $\Upsilon_h = 10$ mrad				
$\Delta \tilde{X}_2$ [μm]	33.94 ± 0.08 [42.7 ± 0.2]	34.16 ± 0.03 [40.7 ± 0.1]	33.82 ± 0.04 [49.1 ± 0.1]	34.66 ± 0.08 [43.7 ± 0.2]
$\Delta \tilde{x}_2$ [μm]	5.65 ± 0.01 [8.56 ± 0.02]	5.39 ± 0.01 [6.49 ± 0.02]	5.38 ± 0.01 [6.48 ± 0.02]	5.66 ± 0.01 [8.40 ± 0.02]
$\Delta \tilde{\varepsilon}$ [μeV]	113.0 ± 0.2 [171.2 ± 0.4]	107.9 ± 0.3 [129.9 ± 0.3]	107.6 ± 0.2 [129.7 ± 0.3]	113.2 ± 0.3 [168.0 ± 0.4]

The results of the studies presented in Fig. 13 provide another example of the superior performance of KB systems compared to Montel and paraboloidal mirrors. However, no optimal f_2 value can be found in any of the considered mirror cases, which would eliminate or mitigate the degradation of the spectral resolution with ε, if the pixel detector is placed perpendicular to the optical axis.

Figures 14 and 15 show the magnitude of the inelastic waist versus deviation from the reference image plane for paraboloidal and Montel mirror systems. These results of the simulations should be compared with the those calculated for the KB mirror systems shown in Figs. 8 and 9, respectively.

Figure 16 shows the performance characteristics of the refocusing systems composed of either paraboloidal or Montel mirrors. These should be compared with the performance characteristics of the refocusing systems composed of KB mirrors in Fig. 10.
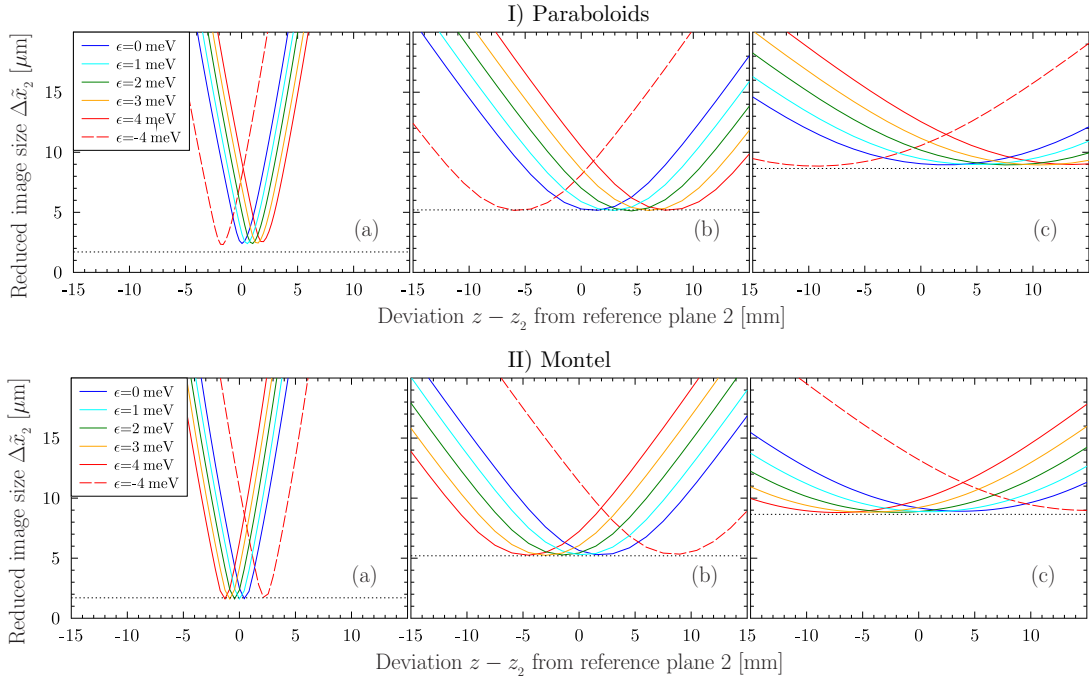
FIG. 14. Reduced vertical image size $\Delta\tilde{x}_2$ as a function of deviation $z - z_2$ from reference image plane 2, calculated for different energy-transfer values ε and for selected focal length values f_2 of imaging mirror F_2: (a) $f_2 = 0.4$ m, (b) $f_2 = 1.471$ m, and (c) $f_2 = 2.5$ m. Presented here are results for (I) paraboloids and (II) Montel mirror systems, with the angular apertures $\Upsilon_h = \Upsilon_v = 1.5$ mrad. All mirror systems feature very similar results. Mirror arrangement corresponds to configuration I in Tables II, III, and VII.
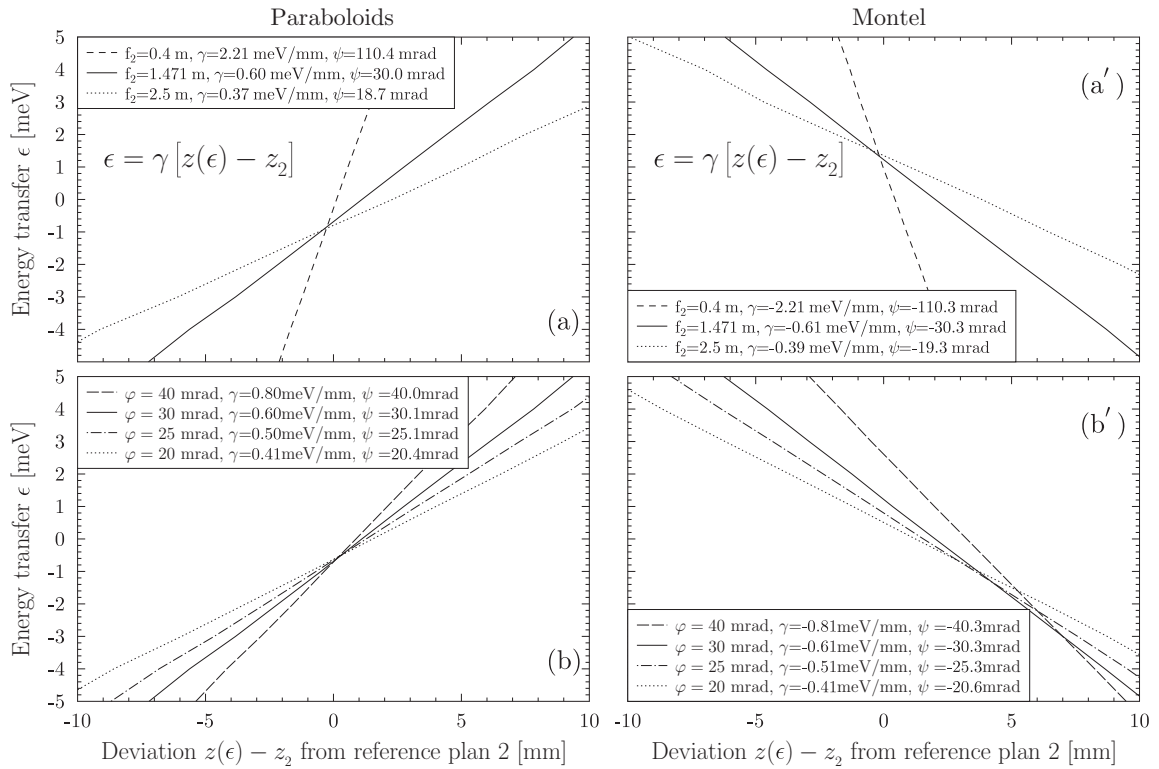

FIG. 15. Correspondence between the energy transfer ε and the deviation $z(\varepsilon) - z_2$ from reference plane 2 of the reduced image with the smallest size. Calculated for the paraboloidal mirrors case (left) and Montel mirrors case (right). Compare with the data for the KB mirrors case in Figs. 9(a) and 9(b). The results are derived from data in Fig. 14 for selected focal length values f_2. Mirrors' incidence angle is $\varphi = 30$ mrad and angular apertures $\Upsilon_v = \Upsilon_h = 1.5$ mrad. (b), (b') Calculated with $f_2 = 1.471$ m (1:1 imaging) and selected values of glancing angle of incidence φ.
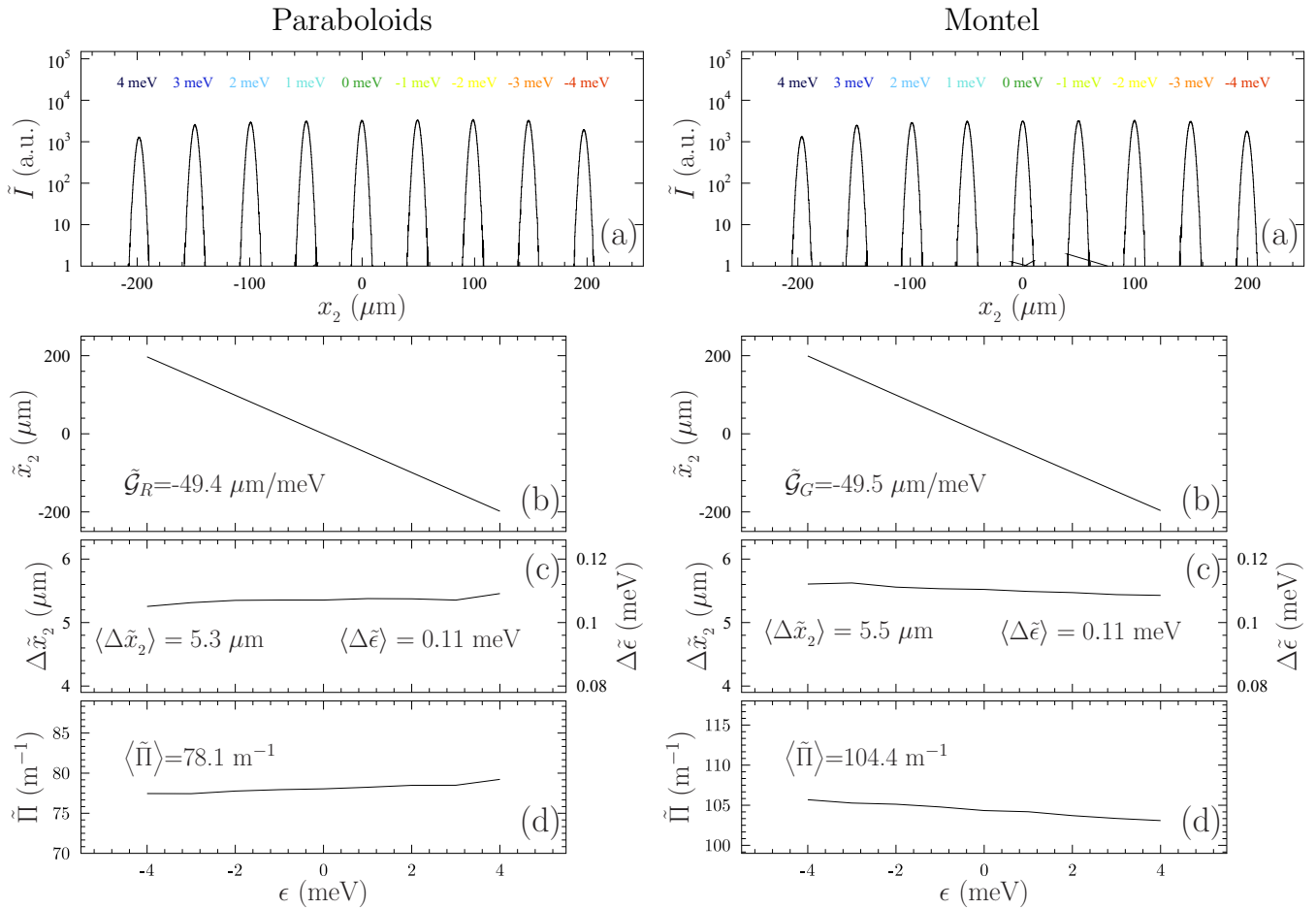
FIG. 16. Performance characteristics of the x-ray echo spectrometer with the refocusing system composed of paraboloidal mirror (left column) and Montel mirror systems (right column): (a) Reduced image profiles calculated for various values of energy transfer ε in inelastic x-ray scattering under the same conditions as in Fig. 7, however with the IXS spectra imaged on the oblique image plane. (b) Image peak position $\tilde{x}_2$, (c) reduced image size $\Delta\tilde{x}_2$, and (d) curvature $\tilde{\Pi}$ of the best-fit parabola to the image profile as a function of ε. Compare with the similar results of Figs. 8 and 2 presented for the case of lenses and KB mirror systems, respectively.

[1] Yu. Shvyd'ko, Phys. Rev. Lett. **116**, 080801 (2016).

[2] *Neutron Spin Echo*, edited by F. Mezei, Lecture Notes in Physics Vol. 128 (Springer, Berlin, 1980).

[3] H. S. Fung, C. T. Chen, L. J. Huang, C. H. Chang, S. C. Chung, D. J. Wang, T. C. Tseng, and K. L. Tsang, AIP Conf. Proc. **705**, 655 (2004).

[4] C. H. Lai, H. S. Fung, W. B. Wu, H. Y. Huang, H. W. Fu, S. W. Lin, S. W. Huang, C. C. Chiu, D. J. Wang, L. J. Huang *et al.*, J. Synchrotron Radiat. **21**, 325 (2014).

[5] A. Q. R. Baron, in *Synchrotron Light Sources and Free-Electron Lasers* (Springer, New York, 2016), pp. 1643–1757.

[6] Yu. Shvyd'ko, Phys. Rev. A **96**, 023804 (2017).

[7] A. Suvorov and Y. Q. Cai, Proc. SPIE **9963**, 99630A (2016).

[8] O. Chubar and P. Elleaume, in *Proceedings of the EPAC-98, ESRF, Grenoble, France* (IEEE, Piscataway, NJ, 1998), pp. 1177–1179.

[9] B. Lengeler, C. Schroer, J. Tümmler, B. Benner, M. Richwin, A. Snigirev, I. Snigireva, and M. Drakopoulos, J. Synchrotron Radiat. **6**, 1153 (1999).

[10] H. Wolter, Ann. Phys. **445**, 94 (1952).

[11] H. Wolter, Ann. Phys. **445**, 286 (1952).

[12] M. Sanchez del Rio, N. Canestrari, F. Jiang, and F. Cerrina, J. Synchrotron Radiat. **18**, 708 (2011).

[13] L. Rebuffi and M. Sánchez del Río, J. Synchrotron Radiat. **23**, 1357 (2016).

[14] L. Rebuffi and M. Sánchez del Río, Proc. SPIE **10388**, 103880S (2017).

[15] Yu. Shvyd'ko, S. Stoupin, K. Mundboth, and J. Kim, Phys. Rev. A **87**, 043835 (2013).

[16] Yu. Shvyd'ko, Phys. Rev. A **91**, 053817 (2015).

[17] T. Matsushita and U. Kaminaga, J. Appl. Crystallogr. **13**, 465 (1980).

[18] M. Sánchez del Río and F. Cerrina, Rev. Sci. Instrum. **63**, 936 (1992).

[19] Yu. Shvyd'ko, *X-Ray Optics: High-Energy-Resolution Applications*, Optical Sciences Vol. 98 (Springer, Berlin, 2004).

[20] H. Yumoto, T. Koyama, S. Matsuyama, Y. Kohmura, K. Yamauchi, T. Ishikawa, and H. Ohashi, Sci. Rep. **7**, 16408 (2017).

[21] P. Kirkpatrick and A. V. Baez, J. Opt. Soc. Am. **38**, 766 (1948).

[22] M. Montel, in *X-Ray Microscopy and Microradiography* (Academic Press, New York, 1957), pp. 177–185.

[23] K. Mundboth, J. Sutter, D. Laundy, S. Collins, S. Stoupin, and Yu. Shvyd'ko, J. Synchrotron Radiat. **21**, 16 (2014).

[24] A. Suvorov, D. S. Coburn, A. Cunsolo, J. W. Keister, M. H. Upton, and Y. Q. Cai, J. Synchrotron Radiat. **21**, 473 (2014).

[25] M. R. Howells, Nucl. Instrum. Methods **177**, 127 (1980).

[26] H. Kogelnik and T. Li, Appl. Opt. **5**, 1550 (1966).

[27] A. E. Siegman, *Lasers* (University Science, Sausalito, CA, 1986).

[28] G. Ghiringhelli, A. Piazzalunga, C. Dallera, G. Trezzi, L. Braicovich, T. Schmitt, V. N. Strocov, R. Betemps, L. Patthey, X. Wang *et al.*, Rev. Sci. Instrum. **77**, 113108 (2006).

[29] P. Delogu, P. Oliva, R. Bellazzini, A. Brez, P. de Ruvo, M. Minuti, M. Pinchera, G. Spandre, and A. Vincenzi, J. Instrum. **11**, P01015 (2016).

[30] G. Monaco, A. Cunsolo, G. Ruocco, and F. Sette, Phys. Rev. E **60**, 5505 (1999).

[31] F. Sette, M. H. Krisch, C. Masciovecchio, G. Ruocco, and G. Monaco, Science **280**, 1550 (1998).

[32] Yu. Shvyd'ko, S. Stoupin, D. Shu, S. P. Collins, K. Mundboth, J. Sutter, and M. Tolkiehn, Nat. Commun. **5**, 4219 (2014).

[33] L. J. P. Ament, M. van Veenendaal, T. P. Devereaux, J. P. Hill, and J. van den Brink, Rev. Mod. Phys. **83**, 705 (2011).